Proton flux variations during Solar Energetic Particle Events, minimum and maximum solar activity, and splitting of the proton belt in the South Atlantic Anomaly

Viviane Pierrard[1], Sylvie Benck[2], edith botek[1], Stanislav Borisov[3], and Alexandre Winant[1]

[1]Royal Belgian Institute for Space Aeronomy
[2]Université Catholique de Louvain
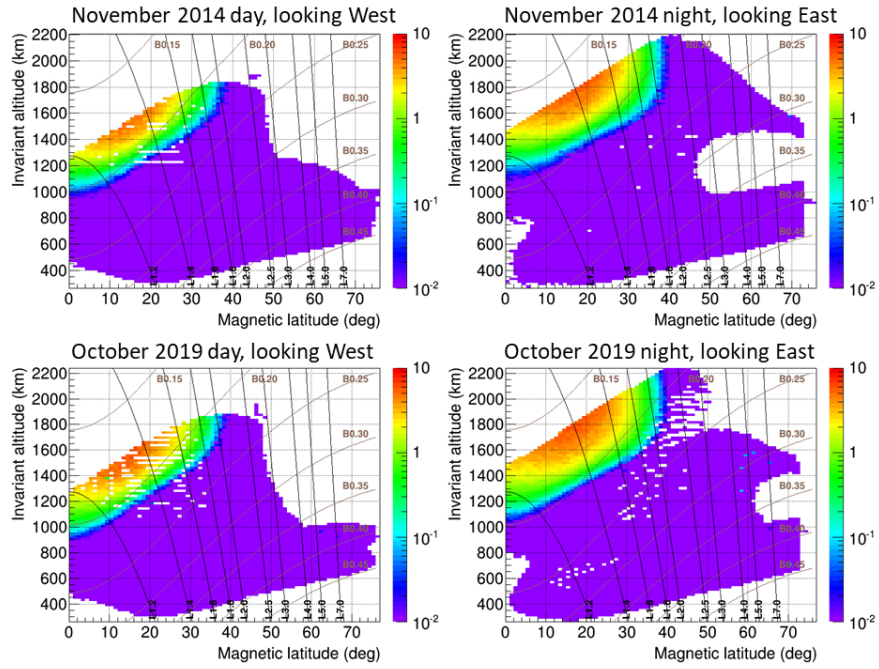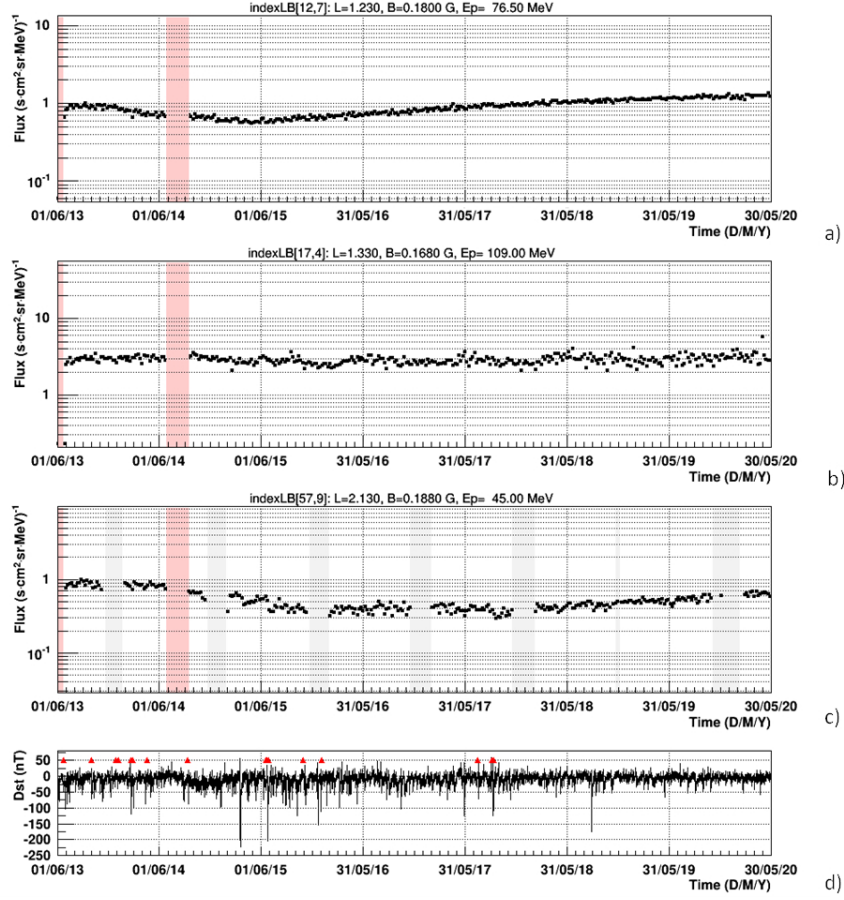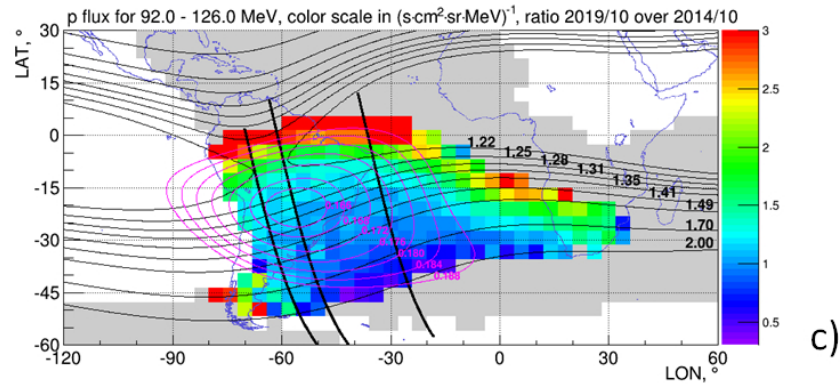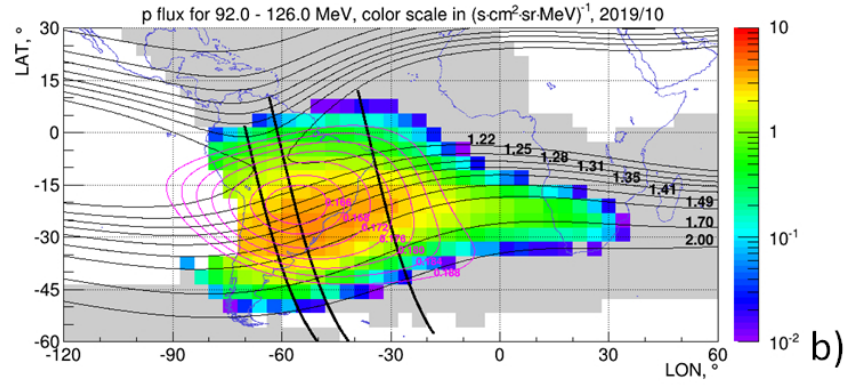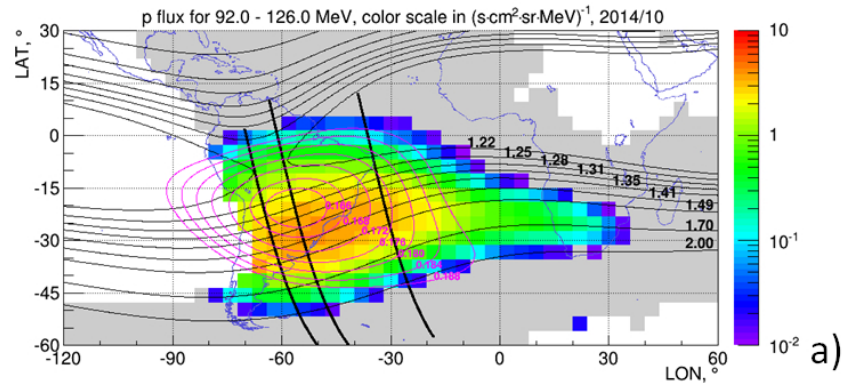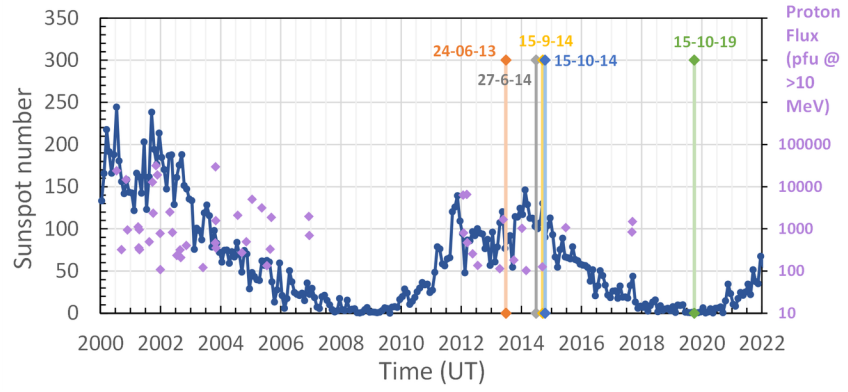[3]Universite' Catholique de Louvain

December 8, 2022

Abstract

The analysis of the proton flux variations observed by the Energetic Particle Telescope (EPT) at energies > 9.5 MeV from the launch of PROBA-V satellite on 7 May 2013 up to October 2022 shows an anti-correlation between the proton fluxes and the solar phase. At solar minimum, the fluxes are higher at low L corresponding to the northern border of the South Atlantic Anomaly (SAA). This solar cycle modulation of the inner belt is mainly due to losses by increased atmospheric interactions during solar maximum.

Strong Solar Energetic Particle (SEP) events, like in January 2014, June 2015 and September 2017, inject energetic protons at high latitudes, but not in the inner belt where protons are trapped at long term at low L. Nevertheless, big geomagnetic storms, including those following SEP a few days after, can cause losses of protons at the outer border of the proton belt, due to magnetic field perturbations.

A double peak in the proton belt is observed during long period of measurements for the EPT channel of 9.5-13 MeV. The narrow gap between the two peaks in the inner belt is located around L=2. This resembles to a splitting of the proton belt, separating the SAA into two different parts, North and South.

The high-resolution measurements of PROBA-V/EPT allow the observation of small-scale structures that brings new elements to the understanding of the different source and loss mechanisms acting on the proton radiation belt at LEO.

indexLB[12,7]: L=1.230, B=0.1800 G, Ep= 76.50 MeV

indexLB[17,4]: L=1.330, B=0.1680 G, Ep= 109.00 MeV

indexLB[57,9]: L=2.130, B=0.1880 G, Ep= 45.00 MeV

November 2014 day, looking West

November 2014 night, looking East

October 2019 day, looking West

October 2019 night, looking East

2

p flux for 92.0 - 126.0 MeV, color scale in $(s \cdot cm^2 \cdot sr \cdot MeV)^{-1}$, 2014/10

a)

p flux for 92.0 - 126.0 MeV, color scale in $(s \cdot cm^2 \cdot sr \cdot MeV)^{-1}$, 2019/10

b)

p flux for 92.0 - 126.0 MeV, color scale in $(s \cdot cm^2 \cdot sr \cdot MeV)^{-1}$, ratio 2019/10 over 2014/10

c)

PROBA-V/EPT proton 13.0 - 29.0 MeV energy range L binned flux time series

PROBA-V/EPT proton 29.0 - 61 MeV energy range L binned flux time series

PROBA-V/EPT proton 61 - 92 MeV energy range L binned flux time series

1 **Proton flux variations during Solar Energetic Particle Events,**

2 **minimum and maximum solar activity, and splitting of the proton**

3 **belt in the South Atlantic Anomaly**

4 Pierrard V.[1,2], S. Benck[2], E. Botek[1], S. Borisov[2], A. Winant[1,2]

5 [1]Royal Belgian Institute for Space Aeronomy, Space Physics and Solar Terrestrial Center of

6 Excellence (STCE), Brussels, Belgium

7 [2]Université catholique de Louvain, Earth and Life Institute, Center for Space Radiations, Louvain-

8 La-Neuve, Belgium

9 Corresponding author: Viviane Pierrard, Royal Belgian Institute for Space Aeronomy, Space

10 Physics and STCE, 3 av. Circulaire, B-1180 Brussels, Belgium (viviane.pierrard@aeronomie.be)

11

14 Key points:

15   1. PROBA-V/EPT reveals that proton flux variations in the SAA are mainly due to losses at

16   low L during solar maximum.

17   2. A splitting of the SAA is observed from 9.5 to 13 MeV corresponding to a double proton

18   belt.

19   3. Big SEP events of June 2015 and September 2017 have small effects in the SAA that is

20   more affected by geomagnetic storms at its outer edge.

21 **Abstract**

22 The analysis of the proton flux variations observed by the Energetic Particle Telescope (EPT) at

23 energies > 9.5 MeV from the launch of PROBA-V satellite on 7 May 2013 up to October 2022

24 shows an anti-correlation between the proton fluxes and the solar phase. At solar minimum, the

25 fluxes are higher at low L corresponding to the northern border of the South Atlantic Anomaly

26 (SAA). This solar cycle modulation of the inner belt is mainly due to losses by increased

27 atmospheric interactions during solar maximum.

28 Strong Solar Energetic Particle (SEP) events, like in January 2014, June 2015 and September 2017,

29 inject energetic protons at high latitudes, but not in the inner belt where protons are trapped at long

30 term at low L. Nevertheless, big geomagnetic storms, including those following SEP a few days

31 after, can cause losses of protons at the outer border of the proton belt, due to magnetic field

32 perturbations.

33 A double peak in the proton belt is observed during long period of measurements for the EPT

34 channel of 9.5-13 MeV. The narrow gap between the two peaks in the inner belt is located around

35 L=2. This resembles to a splitting of the proton belt, separating the SAA into two different parts,

36 North and South.

37 The high-resolution measurements of PROBA-V/EPT allow the observation of small-scale

38 structures that brings new elements to the understanding of the different source and loss

39 mechanisms acting on the proton radiation belt at LEO.

1   Introduction

41 The Energetic Particle Telescope (EPT) is a charged-particle spectrometer using a stack of 12

42 sensor layers including in total 23 silicon detectors that allow to accumulate counts in different

43 physical channels using information from deposited energy in the two front layers (detector S1+S3

44 and S2) in combination with "hit" or "not hit" information from the ten other layers (circular

45 detectors DAM1-DAM10 and corresponding anticoincidence rings) (Cyamukungu et al., 2014).

46 The first layer is subdivided into a central sensor S1 (diameter 3.5 mm) surrounded by an adjacent

47 sensor ring S3 of outer diameter 35 mm. The second layer is composed of one plane circular sensor

48 S2. The proton flux is obtained in 10 virtual channels (there are 10 others for Helium ions and 6

49 for electrons) spanning the energy ranges given in Table 1. The fluxes in each virtual channel are

50 obtained after unfolding of the measured spectra with the efficiency matrix of the detector. It is

51 possible to unfold separately the information obtained with the S1 and S1+S3 sensors.

52 The EPT is accommodated on board the PROBA-V satellite launched on 7 May 2013 on a Low

53 Earth Orbit (LEO), 820 km altitude, 98.7° inclination and a 10:30 – 11:30 Local Time at

2

54   Descending Node (Pierrard et al., 2014). The orbital rotation period of the satellite is 101.21

55   minutes, so that it revolves 14 times around the globe in 24 h. The opening angle of EPT, as defined

56   by the two front sensor layers, is 52° with the central axis pointed East on the night side and West

57   on the dayside. The angle between its boresight direction and the local magnetic field, i.e., pitch

58   angle (PA), varies usually between 60° and 120°, i.e. around 90°, when no off-pointing of PROBA-

59   V is performed for specific operational reasons or some scientific investigations as for example

60   proton pitch angle distribution (PAD) studies (Borisov et al., 2014). The angle between the

61   instrument boresight direction and the local magnetic field is assumed to give the average particle

62   pitch-angle over the field-of-view in the inertial reference system. The standard time resolution of

63   the measurements is two seconds.

64   The position of the satellite is provided by the geographic latitude, longitude and the altitude. The

65   McIlwain L (1966) and local B-field strength are evaluated using the UNILIB v2.20

66   (https://www.mag-unilib.eu/) implementation of the IGRF/Olsen-Pfitzer quiet-time magnetic field

67   model.

Energy channel number	Protons (MeV)
1	9.5-13
2	13-29
3	29-61
4	61-92
5	92-126
6	126-155
7	155-182
8	182-205
9	205-227
10	227-248

68   **Table 1:** Energy ranges corresponding to each resolved virtual channel for protons of the EPT instrument.

69   Previous studies of EPT data focused on electron flux variations during geomagnetic storms

70   (Pierrard and Lopez Rosson, 2016), especially MeV electrons (Pierrard et al., 2019). Proton spectra

71   measured by EPT have been investigated in Borisov et al. (2014), Benck et al. (2016), and Lopez

3

72 Rosson and Pierrard (2017). In the present work, we analyze the variations of EPT proton fluxes
73 over time for different energy ranges. Section 2 presents the time evolution of proton fluxes since
74 PROBA-V/EPT launch and the penetration of energetic protons at high L during SEP events.
75 Yearly changes due to solar cycle are analyzed using maps of the SAA close to solar maximum
76 and minimum in section 3, for high energy protons (>60 MeV) including its effect on East-West
77 asymmetry. The topic of observed effects of SEP and geomagnetic storms on the proton belt is
78 discussed in section 4. The existence of a double-peak structure in the inner belt for the first proton
79 channel (9.5-13 MeV) is studied in section 5. Finally, section 6 discusses the results as compared
80 with other satellite observations and conclusions are provided in section 7.

81 ## 2   Time evolution of proton fluxes since PROBA-V/EPT launch

82 The proton belt is much more stable than the outer (Pierrard and Lopez Rosson, 2016) and inner
83 electron belts (Pierrard et al., 2019). Proton flux variations are slow in the inner belt, with typical
84 time scale around years, but during very intense SEP events, energetic protons are injected at high
85 L during a few days.

86
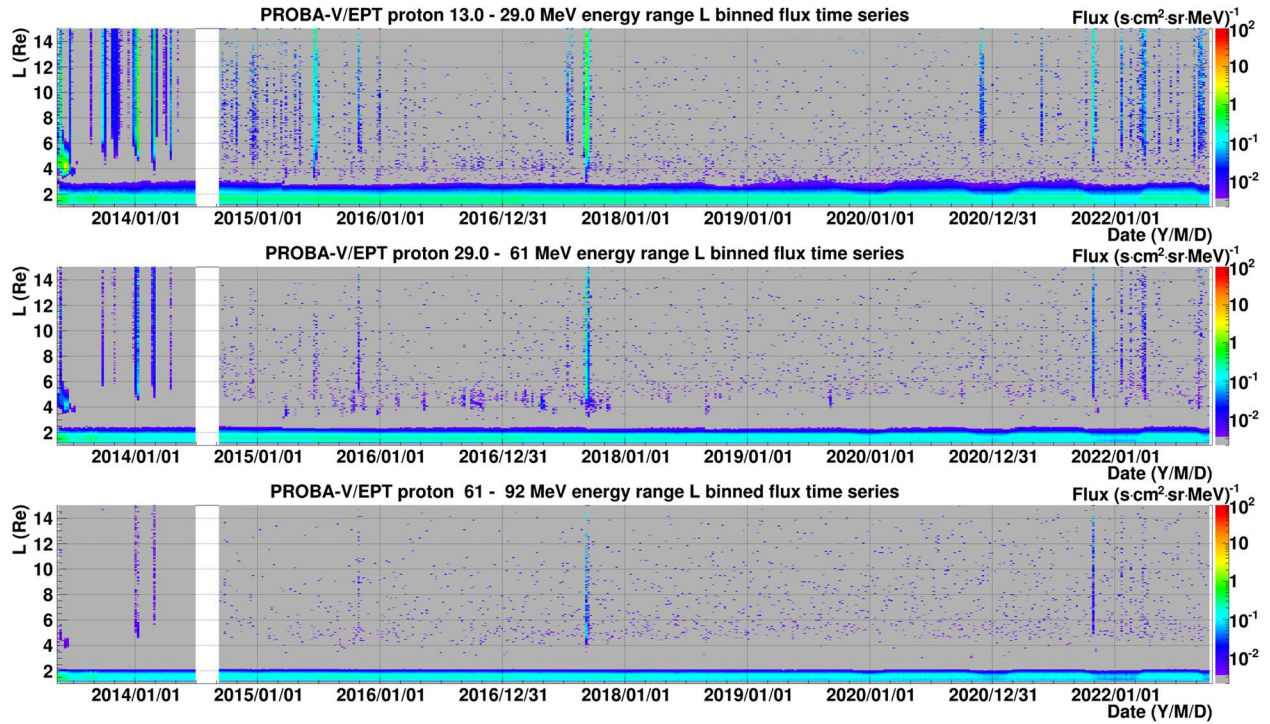
87 **Figure 1.** Proton flux (color scale) observed by EPT in Ch 2 (13-29 MeV, upper panel), Ch 3 (29-61 MeV,
88 middle panel) and Ch 4 (61-92 MeV) (bottom panel) as a function of L and time from 7 May 2013 up to

4

89 October 2022. The vertical white band in the data represents the recalibration period wherein no acceptable
90 data was acquired.

91 Figure 1 illustrates the proton flux observed by EPT from the launch on 7 May 2013 up to October
92 2022, for three selected channels 2, 3, and 4 of energies (13-29 MeV, 29-61 MeV, and 61-92 MeV
93 respectively). The 2D-histograms represent the differential proton fluxes (color scale) as a function
94 of the McIlwain parameter L (y axis) and time (x axis). No EPT data are available during ~2.5
95 months from end June to mid-September 2014 due to a needed recalibration (Borisov and Benck,
96 2019), imposed by a gain change and noise increase in the S3 detection chain. This is represented
97 on Figure 1 by the white region. As consequence, there are some restrictions as to the use of the
98 data (latest dataset available on https://swe.ssa.esa.int/space-radiation):

99   a) Proton channel 1 [9.5-13 MeV] is based on S1+S3 information before 27 June 2014 and
100   on S1 data alone afterwards. As the size of the S1 sensor is about 100 times smaller than
101   the one of S3, the statistics in the channels defined with S1 are very low and the data can
102   only be used within averages (e.g. integration in time) and not as individual 2 second
103   resolution measurements. The field of view is also different which might give changes in
104   the observed proton fluxes if the flux is highly anisotropic.
105   b) After June 2014, the proton channel 2 [13-29 MeV] based on S1+S3 information is highly
106   affected by off-aperture particles and is not usable for detailed studies. This abnormality
107   decreases strongly with energy and becomes definitively negligible for channel 5 [92-126
108   MeV] and higher. In the region where SEP events can be observed (L>3), the lower
109   channels are replaced by "S1-only" data in the dataset with the same limitations as for
110   channel 1 (see Jiggens et al. (2019) for an example of results obtained with averaged "S1-
111   only" data).
112   c) When the flux of >1 MeV electrons is above $2 \cdot 10^3$ cm^{-2} s^{-1} sr^{-1}, electron contamination can
113   be observed in proton channel 2 [13-29 MeV] and 3 [29-61 MeV] (see small vertical stripes
114   in the L=4-5 region from January 2016 to mid-2017, best visible for channel 3).

115 Independent of those caveats coming from the detector itself, other features can be observed on
116 Figure 1 coming from the orientation of the satellite. In fact, during the last winters, starting end
117 2019, the satellite is more often re-orientated for its proper needs in such a way that EPT's pitch

5

118   angle gets far away from its nominal 90° ending up with an average lower flux in the SAA (see

119   dips in the band 1<L<2.5 representing the proton belt).

120   Figure 1 shows that there are proton flux injections at high L only when there are SEP events (see

121   the vertical lines at L>3, in green for the strongest events). While the geomagnetic activity is high

122   during 2015 (Pierrard and Lopez Rosson, 2016), SEP events are observed mainly at the beginning

123   of the EPT flight, more specifically in 2013 and 2014. Later, SEP events are more spaced in time

124   and appear mainly in 2015 and 2017. Note that no strong SEP event occurred after September

125   2017 until October 2022. Very few of these SEP injections barely seem to reach the proton belt

126   extending down to L~3 for channel 1 and at lower L for higher energies (Benck et al., 2016). Some

127   events, especially the two biggest ones of June 2015 and September 2017, inject energetic protons

128   to lower L than the others, and include a strong proton population with energies > 13 MeV (Ch 2,

129   upper panel). For Ch 3 (middle panel), high L injections are observed only in January 2014 and

130   September 2017, and also on 22 May 2013 just after the launch of EPT. Since within a SEP event

131   the flux of protons generally strongly decreases with energy, the channels above 61 MeV (from

132   channel 4 on) are only affected by very strong events. Note that end May 2013, the EPT was still

133   in its commissioning phase and the energy limits for the particle classification were not fully

134   optimized, hence the appearance of a strange shape between L=4 and 5 which is due to

135   misclassified high energy electrons. Later, after the recalibration in September 2014, such

136   structures reappear when the fluxes for electrons with E>1 MeV are above $2 \cdot 10^3$ cm^{-2} s^{-1} sr^{-1}.

137   We show in Table 2 the intensity (in particle flux unit (pfu) at energy > 10 MeV, 1 pfu = 1 p·cm^{-2}

138   ·sr^{-1}·s^{-1}) of the main SEP events observed during the launch of EPT and the most intense events

139   after the year 2000 for comparison (from https://umbra.nascom.nasa.gov/SEP/). One can see that

140   even the most intense SEP in September 2017 is very moderate in comparison to the events

141   appeared in November 2001 and October 2003. In the past, only the very strong SEPs did highly

142   affect the L<3 region due to the injection of energetic protons (Baker at al., 2018). Note that SEP

143   events are not always associated to geomagnetic storms: around 75% of the SEP events from 1978

144   to 2022 are followed by geomagnetic storms with Disturbed Storm Time index Dst < - 50 nT

145   during the next 3 days (Ameri and Valtonen, 2019), but this is not systematic, as shown in the last

146   column of Table 1.

147

6

Start Date	Proton flux (pfu for E > 10 MeV)	Comment	Dst min (nT) in the next 3 days
14 Jul 2000	24000	Very strong	-301 (16 Jul)
04 Nov 2001	31700	Very strong	-292 (6 Nov)
22 Nov 2001	18900	Very strong	-221 (24 Nov)
28 Oct 2003	29500	Very strong	-401 (30 Oct)
22 May 2013	1660		-27 (24 May)
6 Jan 2014	1033		-22 (9 Jan)
21 Jun 2015	1070		-198 (23 Jun)
5 Sep 2017	844		-122 (8 Sep)
10 Sep 2017	1490		-34 (12 Sep)

Table 2. The most intense events with pfu > 15000 after year 2000 (Line 1 to 4) compared with main SEP events (with pfu >800) observed during the launch of EPT (Line 5 to 9).

3   Evolution of proton fluxes in the SAA with the solar cycle

Within this section, we revisit the proton belt as observed by the EPT from the maximum of solar cycle 24 (in 2014) to the following minimum (in 2019) and look what changes it undergoes within this solar cycle phase during the covered time period June 2013-October 2022.

Figure 2 shows the evolution of the average monthly sunspot number from 2000 to 2022, thus including part of the solar cycle 23 and the complete solar cycle 24 that started end 2008 and ended in December 2019 (retrieved from http://www.sidc.be/silso/datafiles). It indicates that the solar activity was around maximum in 2014 and reached minimum in 2019. The purple diamonds in Figure 2 show, for listed SEP events (https://umbra.nascom.nasa.gov/SEP/), the maximum 5 minutes averaged proton (E>10 MeV) fluxes as measured by GOES spacecraft at Geosynchronous orbit.

7
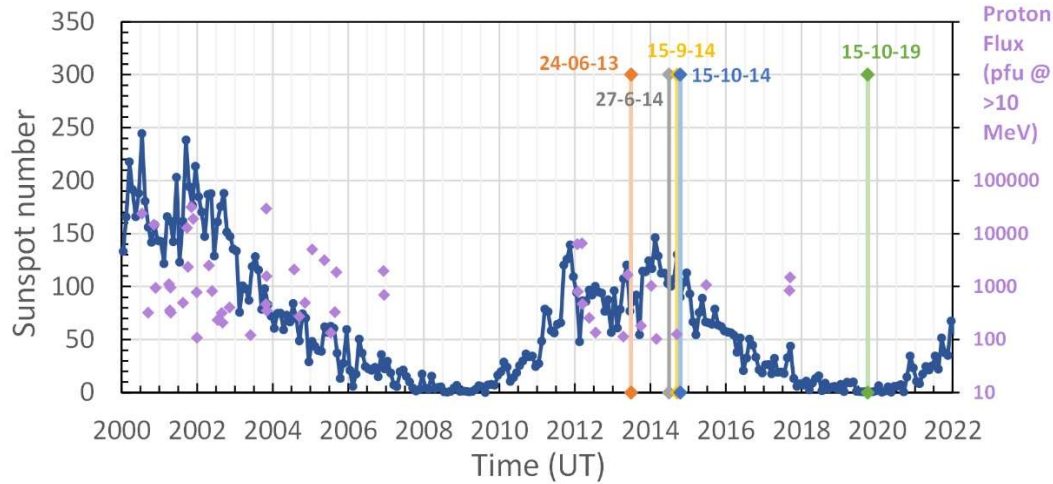
Figure 2. Monthly averaged sunspot number, as a function of time (blue dots connected by continuous blue lines). The purple diamonds show the maximum proton flux as measured by GOES spacecraft at Geosynchronous orbit during each SEP event with pfu>100, with the corresponding scale given by the axis on the right. The fluxes are integral 5-minute averages for energies >10 MeV. Some important dates in the EPT data analysis are also shown (see text).

The nominal period for EPT data acquisition lasts from 24 June 2013 (orange) to 27 June 2014 (grey line), and corresponds to the solar maximum. Many SEP events are observed during this period of 2013-2014. The recalibration period of EPT lasted from 27 June 2014 (grey line) until 15 September 2014 (yellow line). After this period, the declining phase of solar activity started. The minimum corresponds to end 2019 (green line for 15-10-2019) with the new solar cycle 25 starting December 2019. While many geomagnetic storms are observed during this declining period (Pierrard and Lopez Rosson, 2016), only 2 big SEP events are observed, in June 2015 and September 2017. The blue and green lines indicate the middle of two months that are selected for analysis in the next section, i.e., 15-10-2014 (representative of solar maximum) and 15-10-2019 (representative of solar minimum). For these months, the geographical maps of observed EPT fluxes are drawn on Figure 3. This allows us to get a global view on the long-term variation of the proton flux trapped in the SAA at 820 km.

## 3.1 Geographic maps of the flux variations in the SAA for protons with E> 60 MeV

Figure 3 shows the proton fluxes measured by EPT Ch 5 (92-126 MeV) in the SAA, monthly averaged in bins 4° x 4°, for October 2014 (solar maximum) in the upper panel, for October 2019

8

182 (solar minimum) in the middle panel, and the flux ratio 2019/2014 in the bottom panel. The data
183 is shown for night side when EPT is looking East to avoid East-West asymmetry and for boresight
184 orientation 80°<PA<100° to avoid any variation due to steep PAD. This is the reason why different
185 areas have no measurements and are left blank. The (almost) horizontal black isolines correspond
186 to constant L values, with low L close to the equator. The bold (almost vertical) black lines are
187 parts of trajectories showing how EPT crosses the SAA during night passes. The pink ovals
188 correspond to the isolines of the magnetic field (B) intensity, with low values in the center of the
189 SAA.

190 From the bottom panel of Figure 3 showing the flux ratio of 2019/2014, it can be observed that the
191 fluxes at low L (<1.22) and high B, corresponding to the northern border of the SAA, increase by
192 a factor up to times 3 during minimum activity (see red regions). In the same way, the north eastern
193 and western part also show flux increase, but to a lesser extent (see green regions). Thus, from
194 2014 to 2019, the flux increases at low L. On the contrary, in the South part of the SAA, along
195 L=1.7-2, the flux has decreased in 2019 by a factor 1.5-2 (see dark blue region). Here, it must be
196 mentioned that all these regions include flux measurements with low statistics. However, such
197 behavior is observed at all energies above 60 MeV, and also when other months are used provided
198 they are spaced enough in time to make the long-term small variations visible.

199 From 2014 to 2019, the flux at L<1.25 increases in anti-correlation with the solar activity, as shown
200 by the red and green regions corresponding to the Northern part of the SAA. Different spectral
201 characteristics in North and South parts of the SAA were already noted in Pierrard et al. (2014)
202 and Lopez Rosson and Pierrard (2017), but without clear identification of the origin. The observed
203 modulation of proton fluxes at low altitude and at low L associated to the solar cycle seems mainly
204 due to the influence of the atmosphere. During solar maximum (in 2014), the atmosphere extends
205 to higher altitudes and causes more important loss of protons. Atmospheric loss may thus explain
206 the lower fluxes observed in 2014 compared to 2019.

207 In the region of highest L (like L=2) corresponding to the outer edge of the proton belt and the
208 South part of the SAA, the flux at lowest B for high energy protons (E>60 MeV) is on the contrary
209 showing a decreasing trend when going towards solar minimum. This may be related to
210 geomagnetic activity and will be discussed in more detail in section 4.

9
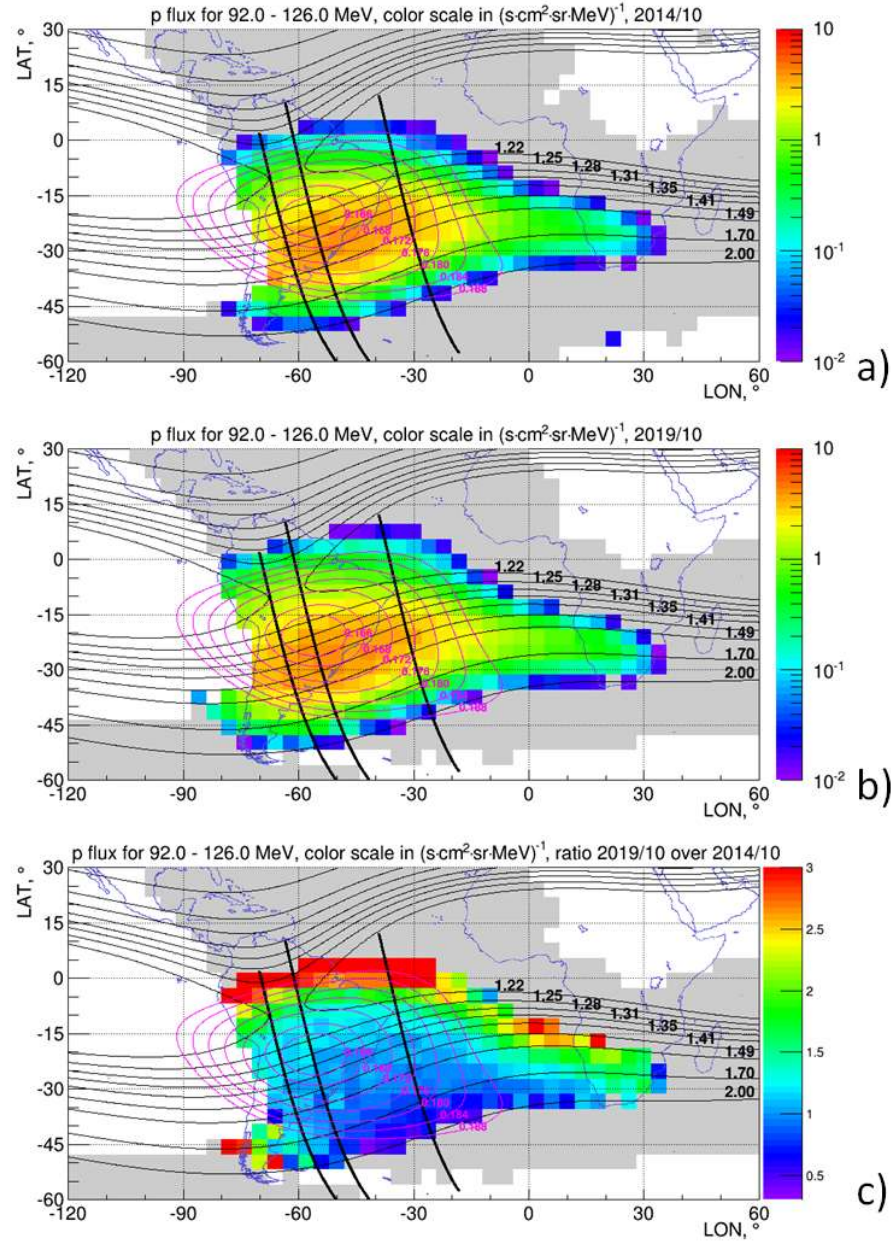
Figure 3. Geographical maps of the monthly averaged proton flux in Ch 5: a) October 2014, b) October 2019, c) ratio of 2019 data divided by 2014 data. The bold black lines are parts of trajectories showing how EPT crosses the SAA during night passes from south to north. The grey areas are those where the fluxes are below minimum, i.e. 10^{-2} $s^{-1}cm^{-2}sr^{-1}MeV^{-1}$, and the white areas are those where no data fulfill the selection criteria: night side data with boresight orientation 90°±10°. Iso-L lines and Iso-B lines are shown by black and pink lines respectively.

The observation of the atmospheric effect is in good agreement with other long-term measurements at low-Earth orbit (LEO) like SAMPEX (Heynderickx et al., 1999, Pierrard et al., 2000) or POES

10

220   (Li et al., 2020), for which clear solar cycle variations of the proton fluxes are observed and anti-
221   correlate with the solar activity marked by the sunspot number. The atmospheric density varies
222   with the 11-year solar cycle so that the low L proton population is lower during high solar activity.
223   The solar cycle modulates the flux at the border of the SAA. During solar maximum the flux
224   decrease is mainly due to this enhanced atmospheric loss.

225   In addition to the lower extension of the atmosphere during solar minimum, the slow increase of
226   radiation belt proton fluxes from 2014 to 2019 may also be influenced by Cosmic Ray Albedo
227   Neutron Decay (CRAND) (Selesnick et al., 2014). Galactic cosmic rays (GCR), mostly protons
228   with E>100 MeV produced by supernovae in our galaxy interact with neutral atoms in the upper
229   atmosphere to produce energetic albedo neutrons which decay into protons, electrons, and
230   antineutrinos (Li et al., 2021). Because they are electrically charged, some of these electrons and
231   protons become geomagnetically trapped at low altitude in the inner belt region. Due to their higher
232   mass, most of the kinetic energy is retained by the protons. That is why the protons trapped in the
233   radiation belt are so energetic. GCR are detected by neutron monitors at the surface of the Earth.
234   They show a variation in cosmic rays on the 11-year sunspot cycle, modulated by the solar wind.
235   GCR are more intense during the quiet period of 2018 and 2019, so that this source mainly explains
236   the increase of the fluxes. Nevertheless, the magnitude of the flux variation is much greater than
237   the solar cycle variation of galactic cosmic rays (>GeV) that are the source of these trapped protons
238   (Li et al, 2021), so that effects of the terrestrial atmosphere seem to dominate in the solar cycle
239   modulation at low altitude.

240   **3.2   Modulation with solar phase: shifted anti-correlation**

241   Figure 4 shows the time evolution of the flux in three bins corresponding to different parts of the
242   SAA. Different energies are selected to show that the trend is observed over a large energy range.
243   The first bin is located at the top border of the SAA at low L=1.23 and B=0.18 (top panel). The
244   flux shows a clear anti-correlation with the solar cycle, thus is at minimum in 2014-2015 and
245   slightly increases until 2019. The second bin is located in the center of the SAA (L=1.33, B=0.168)
246   (second panel). No long-term variation is observed in this bin. The flux variations seem to be
247   limited to the boarders of the SAA. At the southern border of the SAA corresponding to higher L
248   (L=2.13 in the third panel), the flux is anti-correlated with the solar cycle but with a larger time

11

delay, the minimum being observed during a longer period than in the northern border. At high L, the flux continues to be low up to mid-2018 when it starts to increase.

Note that here again, a selection has been made to avoid the effects of the East (night) and West (day) directions of the instrument: i) boresight orientation, i.e. PA of the viewing direction with respect to the magnetic field between 80° and 110°; ii) only night side data is included, i.e., EPT is looking East. For dayside data (EPT looking West), the viewing direction of EPT does mostly not fulfill the PA condition.

12
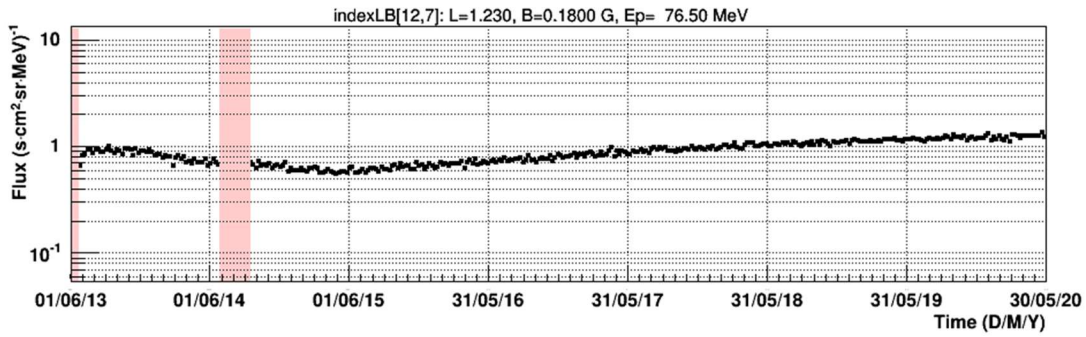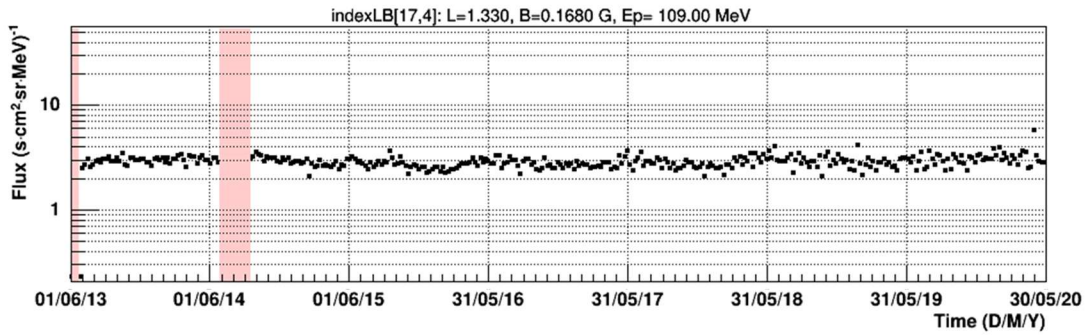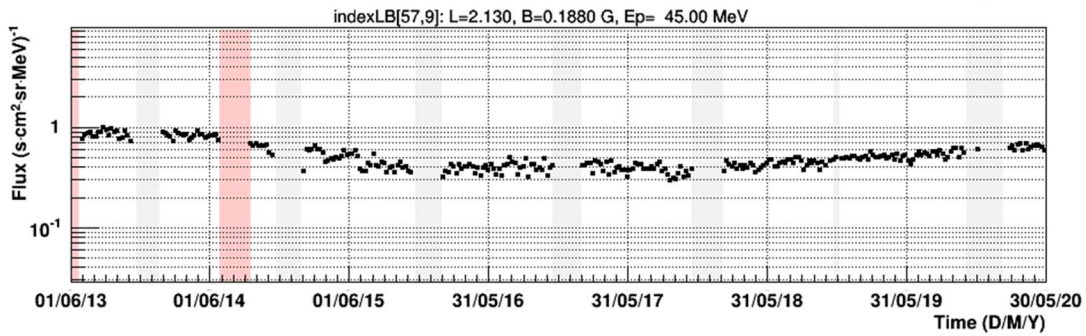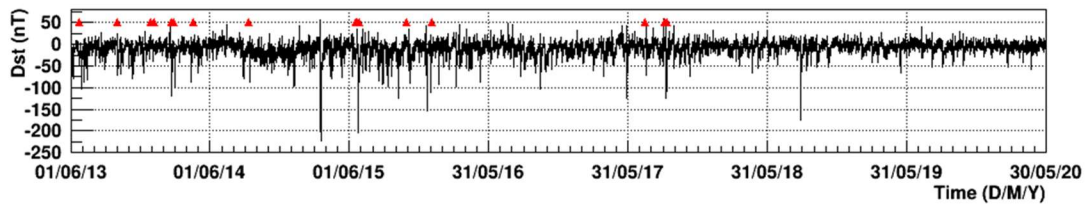
257 **Figure 4.** Time series of proton flux (weekly averages) in the SAA at three different positions for different
258 energies. One from the northern border at low L=1.23 (a), one from center at L= 1.33 (b) and one from the
259 southern border at L=2.13 (c). The fluxes present night-side data with boresight orientation 90°±10°. The
260 pink bands indicate the time periods where the EPT was in its commissioning phase or recalibrated. The
261 grey bands highlight the time periods where no data exist for the pitch angle selection. The bottom panel
262 (d) shows Dst as a function of time and the red triangles indicate the occurrence of SEP events.

263 ## 3.3   Atmospheric effect and East-west asymmetry

264 Figure 5 shows maps of proton flux as a function of the invariant altitude (location of the mirror
265 points) vs magnetic latitude for November 2014 (top panels) and October 2019 (bottom panels).
266 This coordinate system was introduced by Cabrera and Lemaire (2007) to map the radiation belt
267 fluxes in the low-altitude environment. Left panels correspond to west direction, right panels to
268 east direction. The figure shows that the mirror points are lower, i.e. have a lower invariant altitude,
269 when looking west and during solar minimum (bottom panels), although less pronounced. This
270 can be observed especially for the lowest L values (see the invariant altitude line 1200 km for
271 instance). This illustrates that it is important to not mix east- and west-looking data for energetic
272 protons at low orbit.

13
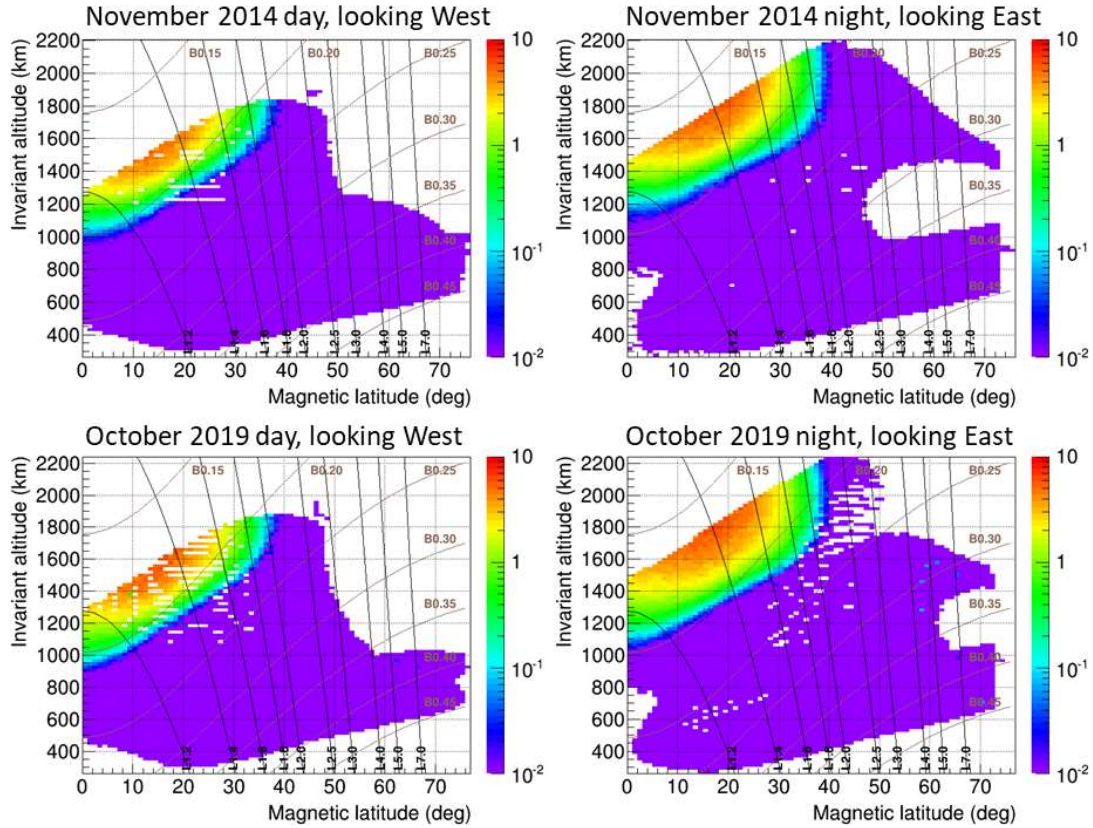
Figure 5. Invariant altitude versus magnetic latitude map for proton channel 4 [61-92 MeV]. Top left panel: November 2014 day, looking West, Top right: November 2014 day, looking East, Bottom left: October 2019 day, looking West, Bottom right: October 2019 day, looking East. The isolines of L and B are also shown in black and brown respectively.

At low altitudes, the high-energy trapped proton fluxes are strongly anisotropic because they are controlled by the density distribution of the Earth's atmosphere that induces a steep pitch-angle distribution. The East-West effect caused by the finite size of the proton gyration radius was already pointed by Kruglanski (1996) for instance.

Figure 6 illustrates the averaged proton fluxes measured by the EPT as a function of B/B_0 where $B_0 = 0.311653 / L^3$. It shows that the East-West asymmetry is strongest for low L values (top panels) and increases with energy (right panels). While for the lowest L, both regime regions (cf. blue curve with two slopes) are affected by the solar phase change, showing higher flux at solar minimum, at high L only the fluxes in the region where atmospheric interactions are dominant are significantly increased during solar minimum.

14
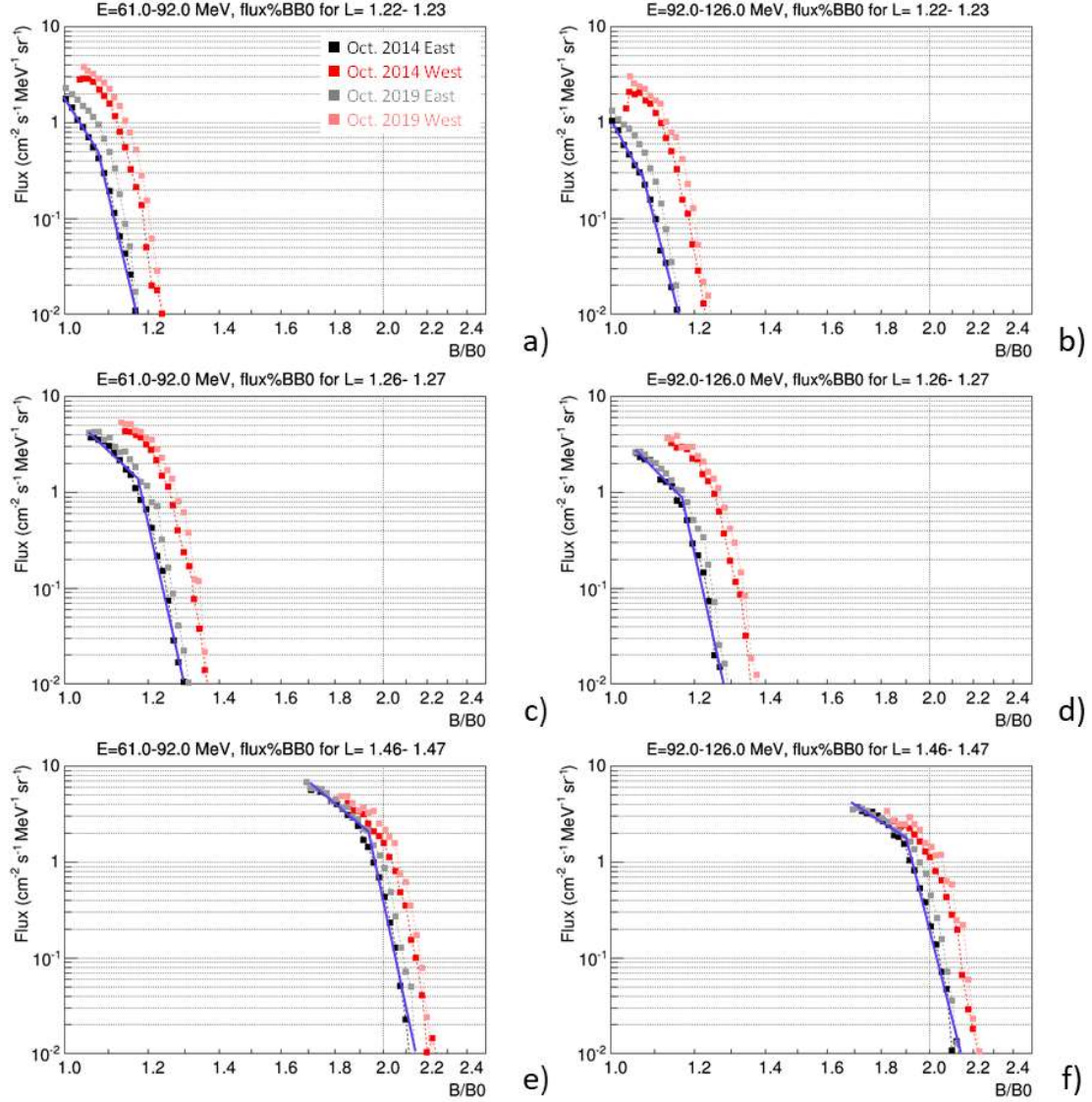
Figure 6. For two time periods (October 2014 and October 2019), for the two orientations of the satellite (West in red, East in black), averaged proton fluxes measured by the EPT in the 61-92 MeV (left panels) and 92-126 MeV (right panels) energy channel for L=1.22-1.23 (top panels), L=1.26-1.27 (middle panels) and L=1.46-1.47 (bottom panels) as a function of B/B_0. The two-slopes blue line across black points (night time measurement) aims to show the two regimes of dominant proton interactions: with magnetic field (at lower B/B_0) and upper atmosphere (at higher B/B_0).

3.4 Pitch angle distribution

The particle flux is nominally reconstructed within the isotropic flux assumption, i.e., the efficiency matrix is simulated by assuming isotropic flux at the aperture. But the higher the proton energy, the narrower the Field of View (FOV), i.e., FOV=52° as defined by the front sensor

15

299 "S1+S3" and second sensor S2 (for the first channel 9.5-13 MeV) and FOV=35° as defined by

300 "S1+S3" and the 4th DAM (for the channel 92-126 MeV) (Cyamukungu et al., 2014).

301 So with EPT, especially for the high energies, the flux corresponds much closer to the J(90°) flux

302 (with $J(\alpha)=J(90°) \cdot \sin^n(\alpha)$, α is the pitch angle) rather than to omnidirectional flux, hence the higher

303 flux levels observed.

304 If the dominant interaction is with the magnetic field, then assuming $J(\alpha)=J_0 \sin^n(\alpha)$ for PAD (here

305 $J_0= J(90°)$) and $\sin^2(\alpha_0)=\sin^2(\alpha) B/B_0$ (where α_0 is the equatorial pitch angle), one can express the

306 flux in this form:

307 $J(\alpha)=J_0 \sin^n(\alpha_0) (B/B_0)^{-n/2}$

308 The distribution of $J(\alpha)$ versus B/B_0 in log-log scale is located around a line with a slope -n/2, for

309 instance on Figure 6, this corresponds to the slope of the left part of the blue curves. The n values

310 obtained here are of the order of 20 but with very high uncertainty. Given the imprecision that

311 arises from this method, it was not possible to perform any study of change in PAD with the solar

312 cycle. A detailed study of PAD based on targeted re-orientation of the satellite in 2014 can be

313 found in Borisov et al. (2014).

4   Effects of SEP and geomagnetic storms

315 Within this section, we revisit the proton population as observed by EPT from June 2013 – October

316 2022 and look at how the proton belt is affected by geomagnetic activity and SEP events during

317 that time period.

318 Geomagnetic storms following SEP may have an effect on the outer edge of the proton belt, as it

319 can be observed in Figure 7 (see upper panel) which shows proton data during the strongest

320 geomagnetic storm (Pierrard and Lopez Rosson, 2016) of solar cycle 24, appearing on 17 March

321 2015, reaching a Dst index of -223 nT (Figure 7c, Dst data retrieved from https://wdc.kugi.kyoto-

322 u.ac.jp/). One can see in Figure 7a that it is associated to a SEP event of small intensity arriving a

323 few days before and injecting protons of E<50 MeV at high L. The data from figure 7b represents

324 pass-averaged flux time series derived from EPT, a pass starting when L>6 over a polar region

325 (data downloaded from https://swe.ssa.int/space-radiation). This event was not reported as a

16

326 SEP event (on https://umbra.nascom.nasa.gov/SEP/), because the flux is lower than the threshold

327 of 10 p$^+$ cm^{-2}s^{-1} sr^{-1} that has been chosen to register the SEP event within the database. In fact, it

328 appears as very faint event in Figure 7a as compared to other SEP events appearing during the

329 flight of PROBA-V.

330
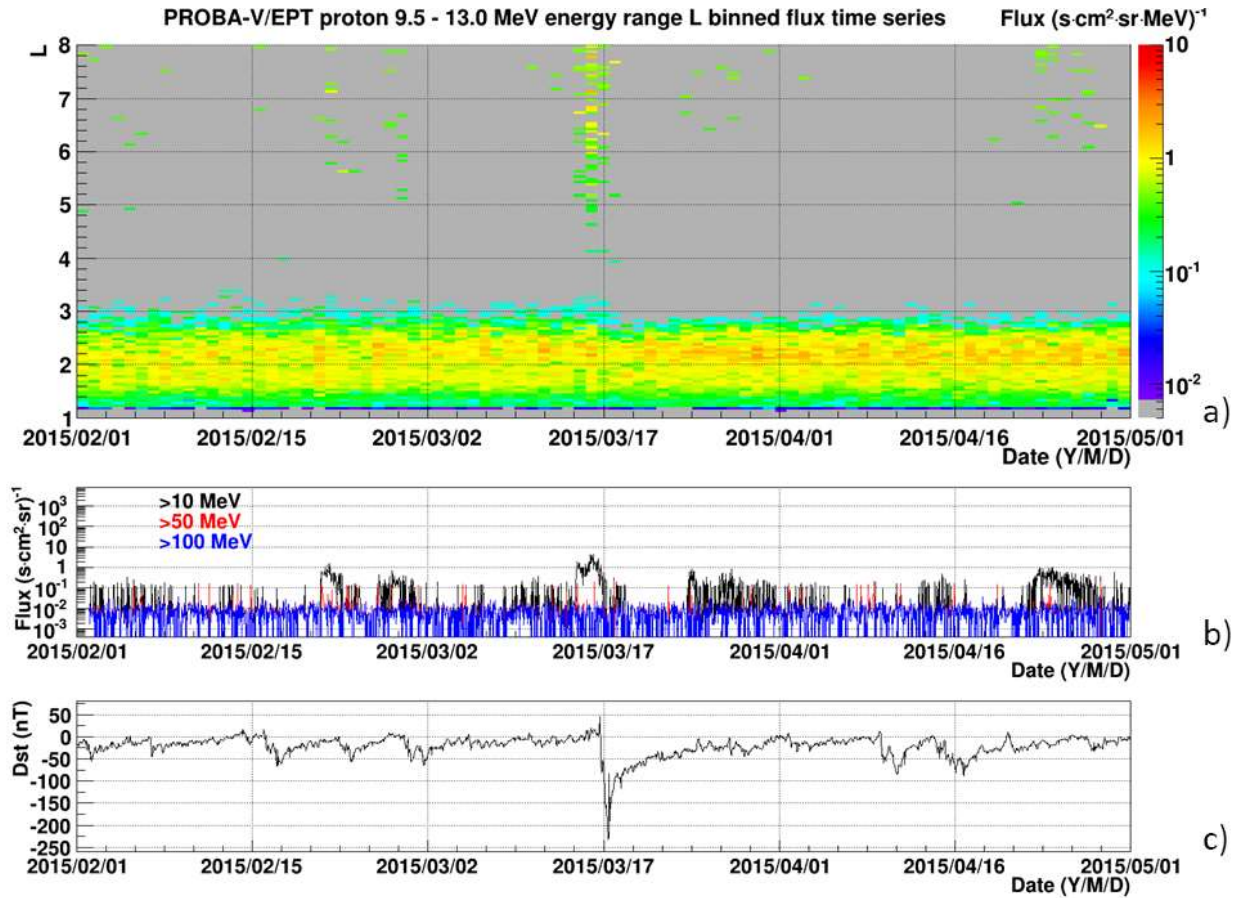
Figure 7. a) Proton differential flux observed by EPT in Ch 1 (9.5-13 MeV) as a function of L and time
332 from 1st February to 1st May 2015 (upper panel). The bin size in L is 0.05 and the bin size in time is 1 day.
333 b) The EPT derived integral fluxes for protons of E>10 (black), > 50 (red), and >100 MeV (blue) for the
334 same time period. c) Dst variation showing the up-to-now largest Dst decrease during PROBA-V mission.

335 The SEP injection of protons at high L values started on 15 March 2015, thus a few days before

336 the geomagnetic storm started, with a strong Dst decrease during the night from 16 to 17 March.

337 The SEP injection did barely reach the L=4 region. However, in combination with the on-set of

338 the storm, the reduction of the outer edge of the inner proton belt, decreasing suddenly from L=3

339 to L=2.7 associated to the compression of the magnetic field during the storm can clearly be

340 identified.

17

341   A similar decrease of the outer edge of the proton belt is also seen during the event of September

342   2017 (Figure 8). Panel a) shows that this SEP event is much more intense than the 2015 event and

343   that even protons of energy > 100 MeV are observed (Figure 8b). For the energies < 30 MeV, SEP

344   protons reach down to L~3. The day when they reach their minimum L corresponds to the time

345   period when the geomagnetic storm reaches its second minimum. When Dst decreases, the

346   magnetic field is compressed and allows the energetic protons to penetrate at lower L. Associated

347   to this easier access of SEP protons at low L, inner belt protons are nevertheless lost at its outer

348   edge. This has been observed previously: depending on the magnetic compression and SEP

349   injections, additional protons can be trapped in the inner belt or on the contrary protons can be lost

350   (Selesnick et al., 2010). The limit of the magnetic trapping of the protons depends on the gyration

351   radius of the protons that has to be sufficiently low to have a periodic motion (Maget et al., 2013).

352   For the protons that have a high gyration radius in comparison to electrons due to their higher

353   mass, violation of the center guide approximation happens to protons during compression times of

354   the magnetic field (Pierrard et al., 2020). This results in their loss at the outer edge of the proton

355   belt, here essentially observed for protons of Ch1 and Ch2, because their edge is at L>2.5 and their

356   fluxes are relatively high. In fact, the sensitivity in flux of EPT for higher energies may be a reason

357   that such phenomena cannot be observed for E>30 MeV, yet it cannot be excluded that the

358   depletion in flux as observed at higher L in Figure 3 comes from multiple erosion events occurring

359   during solar declining phase and that annihilates somehow the flux increase due to changes in

360   extension of the atmosphere, especially that those particles have the largest gyration radius.

18
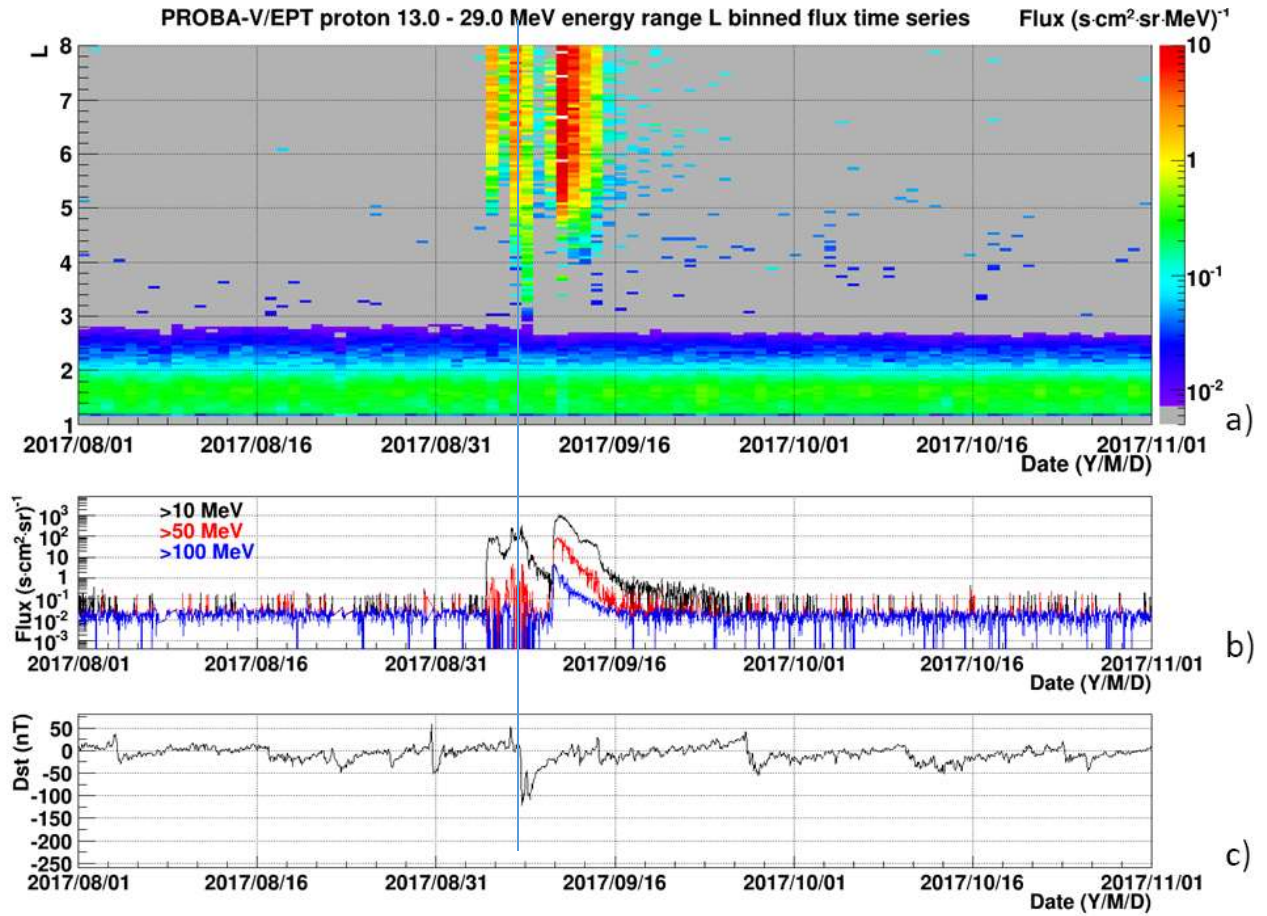
Figure 8. a) Proton differential flux observed by EPT in Ch 2 (13 - 29 MeV) as a function of L and time from 1st August to 1st November 2017. b) The EPT derived integral fluxes for protons of E>10, >50 and >100 MeV and c) the Dst variation for the same time period.

Accordingly, such losses can be attributed to the disruption of the adiabatic particle motion due to distortion of the magnetic field, specifically by increase of the field line curvature. Such losses due to the magnetic field perturbation can happen even without significant SEP event, only due to geomagnetic storms that can be generated by other solar events not including energetic particles, like Corotating Interaction Regions (CIR) for instance (e.g. Rouillard et al., 2021 for a review) . The maximum L of trapped protons, i.e. the extension of the proton belt, can be related to the trapping limits estimated from magnetic field line curvature. Rapid magnetospheric compression can cause solar proton injections and radial shift of preexisting trapped protons (Selesnick et al., 2010).

19

374   For the two events shown here, it could be observed that the loss of radiation belt border protons

375   was higher for the 2015 event than for the 2017 event, linked certainly to the higher intensity and

376   hence compression within the 2015 storm.

377   5   Structures in the SAA at low proton energies

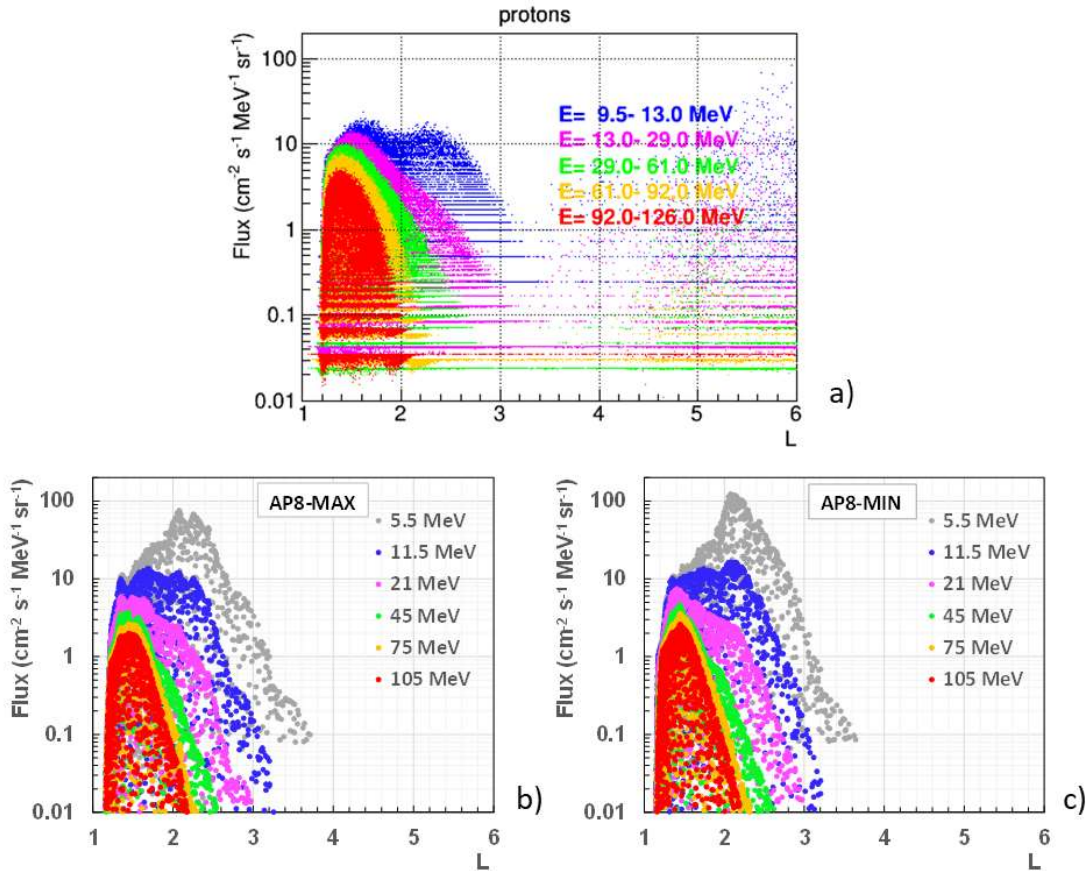378   Within this section a special feature observed at low proton energy < 15 MeV will be emphasized.

379

380   Figure **9**a shows 2-second resolution data taken along the orbit as a function of L for the region

381   1<L<6 (all B included) during the time period 1/1/2014-31/3/2014. On this graph, the coverage of

382   the 9.5-13 MeV protons of EPT (blue dots in top panel) is particular because it registered the

383   presence of two peaks separated by a little dip around L=2. This phenomenon is observed

384   immediately after the launch of PROBA-V and during all the observation period, but only for this

385   low energy channel. The points observed above L=4 originate from a SEP event that occurred

386   during January 2014.

20

387 The double peak is unexpected because it is not clearly obtained by the AP8 model (Vette, 1991),

388 as   illustrated   in   the   bottom   panels   of
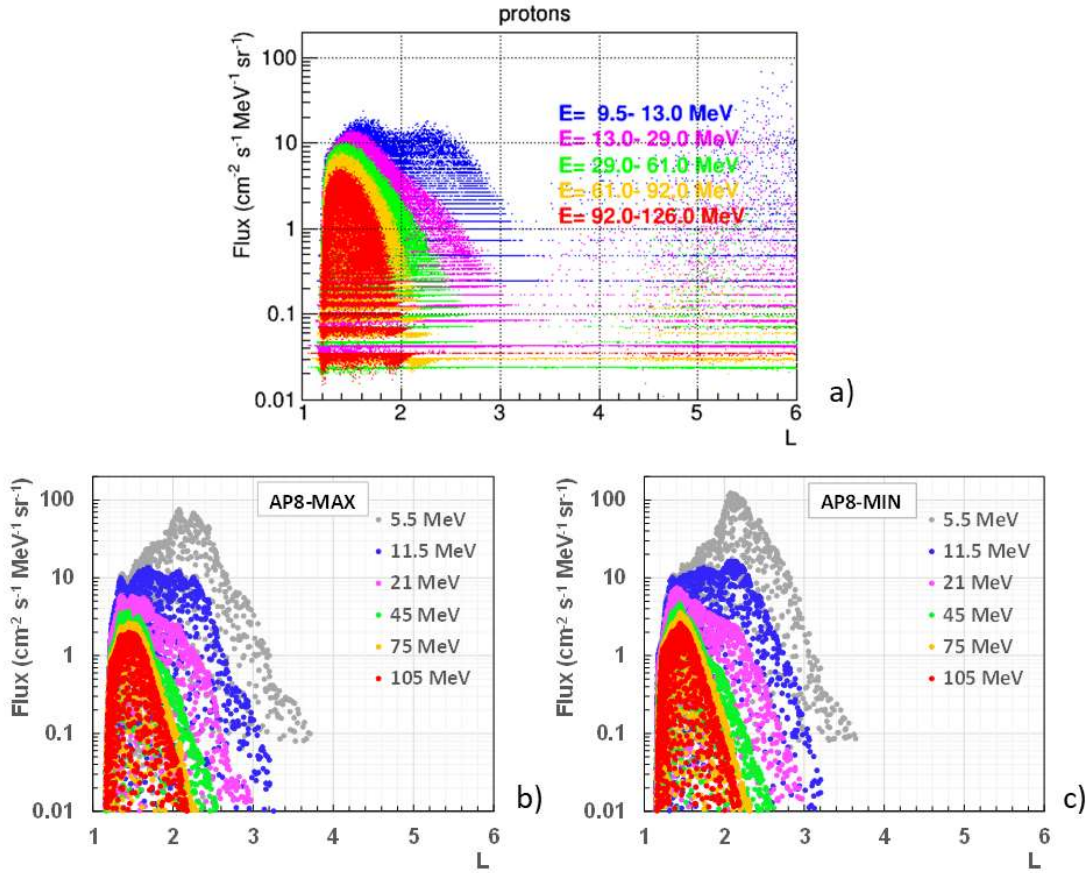
389

390 Figure **9** for maximal (panel b) and minimum (panel c) solar activity. These panels show the

391 differential proton flux as a function of L as calculated from runs on SPENVIS

392 (www.spenvis.oma.be/) for a helio-synchronous polar orbit at 820 km altitude, for different

393 energies corresponding to those of EPT channels. Note that AP8 predicts omnidirectional integral

394 fluxes, and hence the differential unidirectional (per steradian) fluxes are calculated from the AP8

395 model. In addition, some difference in absolute height may appear, also due to the fact that the

396 higher the proton energy in EPT, the lower the FOV within which the particles are detected.

21
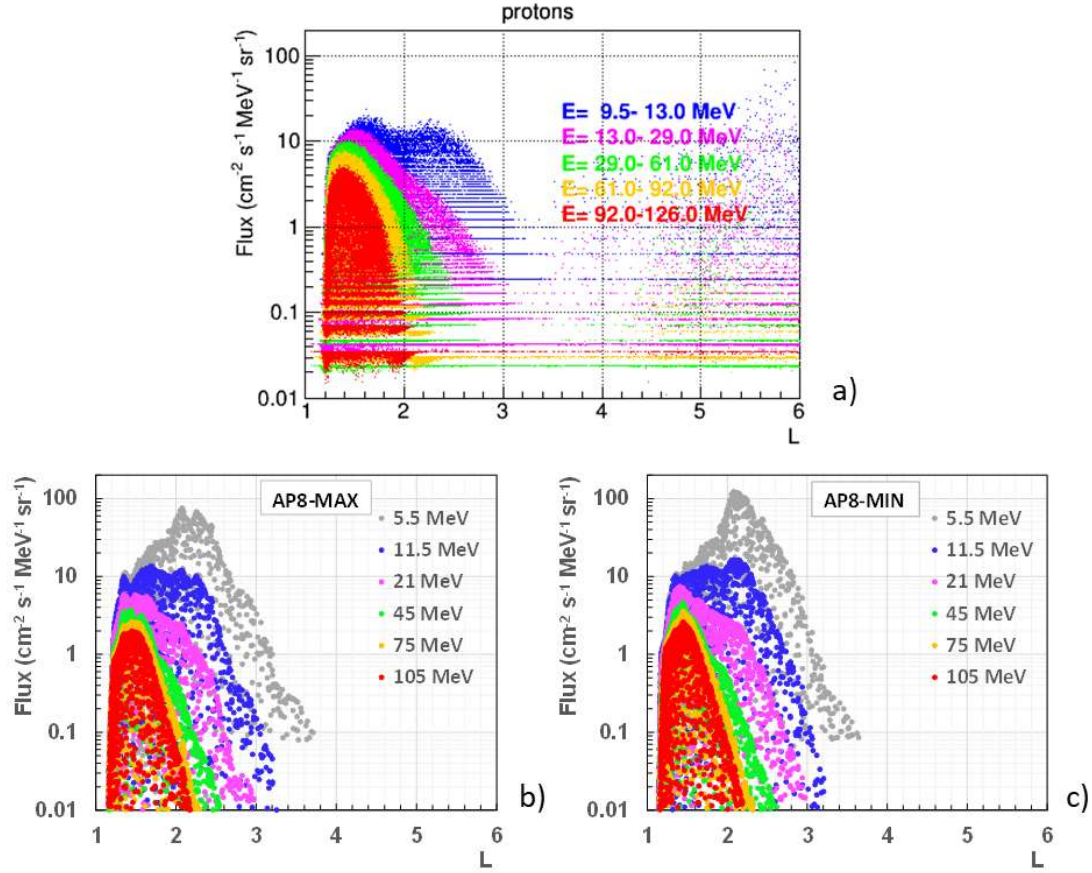
Figure 9. Top panel: Differential 2-second resolution proton flux as a function of L as observed by the EPT on-board PROBA-V (time period 1/1/2014-31/3/2014). Bottom panels: Differential proton flux as a function of L as result of the AP8-MAX b) and AP8-MIN c) model (Vette, 1991), from a run on SPENVIS for a helio-synchronous polar orbit at 820 km altitude.
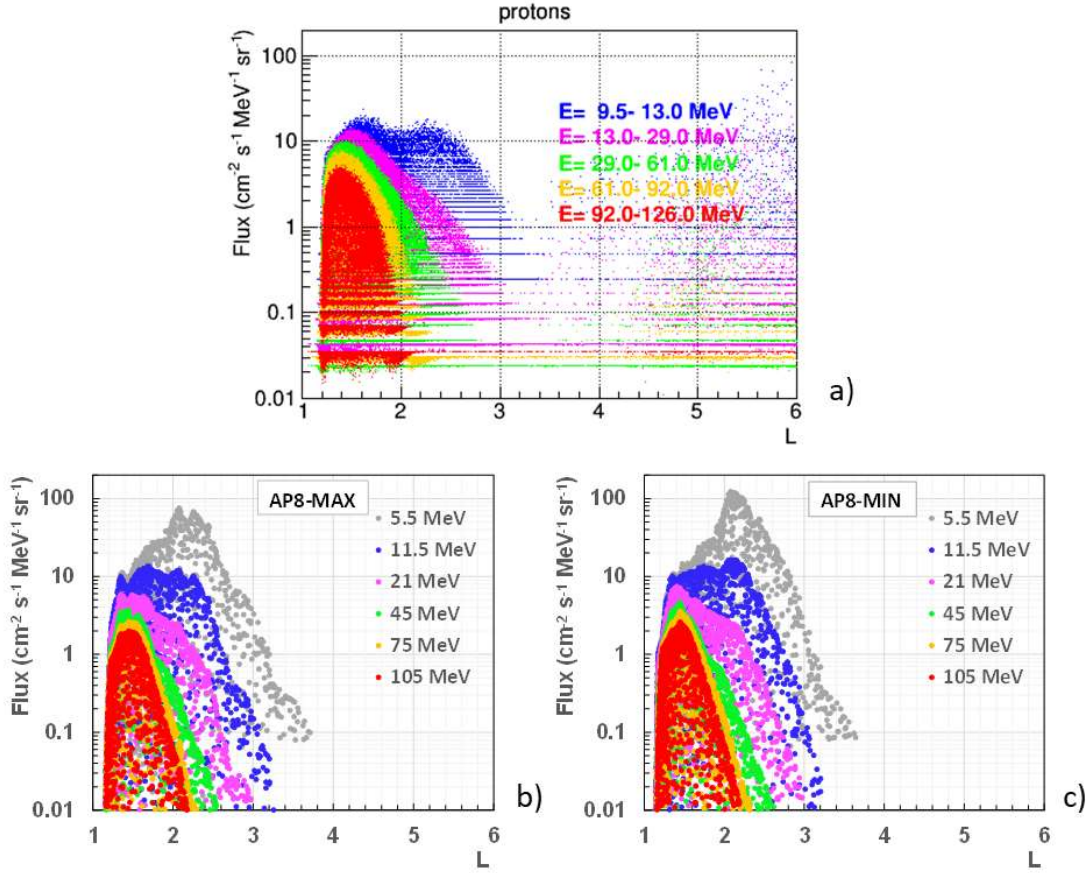
402

Figure **9**a suggests that there are two populations within the proton belt: 1) the population below L=2 where the high energy protons are also significantly present and the proton spectra are relatively flat and 2) the population above L=2 where the low energies below 10 MeV largely dominate and the proton spectra are rather steep. The origin may be either different source of particle production, different loss processes or a combination of both. More information about this is given in the discussion section 7.

The second peak in Ch 1 (at L>2) looks like an "additional" belt in the South part of the SAA, as illustrated in the map on Figure 10. In the top panel, corresponding to Ch 1, the South part of the SAA is more extended (see the red region that extends up to L=3) than what is observed in higher energy channel (see bottom panel for Ch 2 in Figure 10). For the proton channel E=9.5-13 MeV (upper panel), a slight valley can be observed in the region L~2. For the proton channel E=13-29 MeV, the flux in the region L>2 has significantly decreased. The black lines show ascending trajectories of the EPT when traversing the SAA.

23
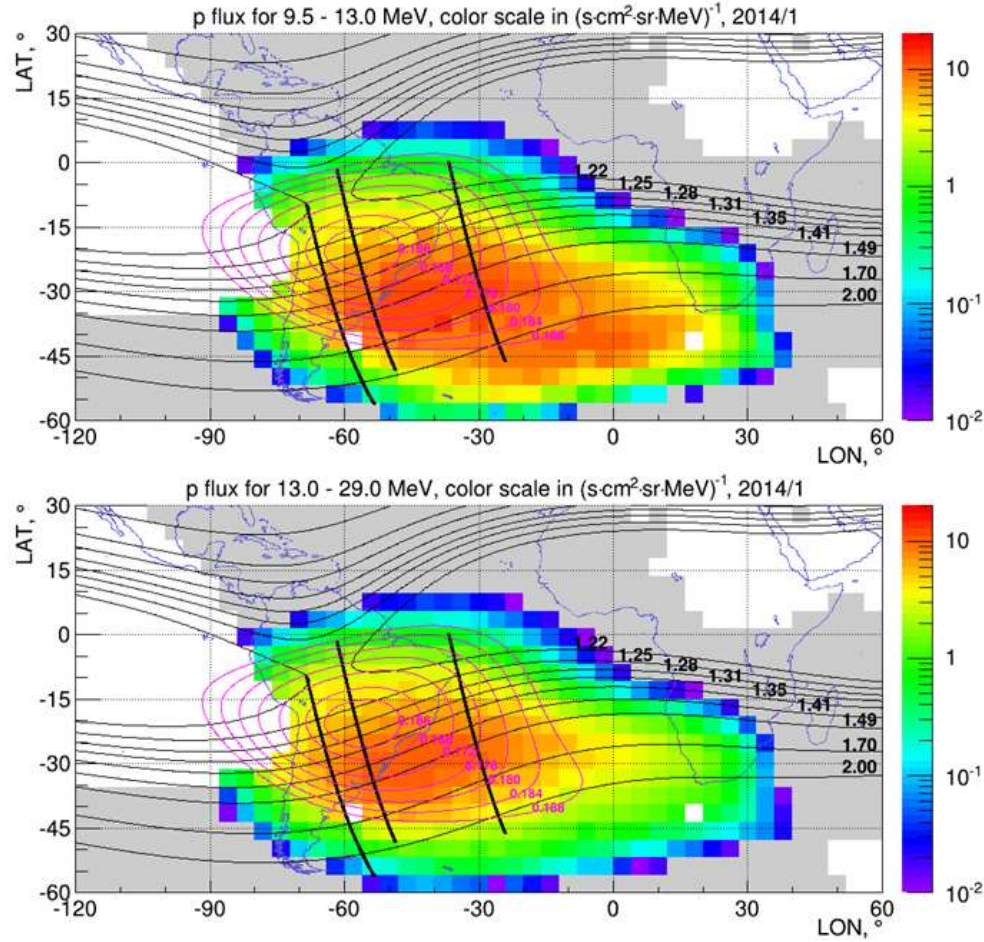
Figure 10. Geographical maps of the SAA, observed in January 2014 by EPT for two proton energies: Ch 1 (9.5-13 MeV, top panel) and Ch2 (13-29 MeV, bottom panel). Nightside data with boresight orientation 90°±10° were selected.

The particularity of the SAA southern region gets even more highlighted when looking at Figure 11. Note that this time the analyzed data come from the period after recalibration of the EPT and therefore the channel 1 data is based on information when the protons has passed only through S1 and then hit S2. The statistics in the channel after 2 second integration time is very low and therefore the average is done over a longer period than for Figure 10, i.e. 2 months. Also, to get a coherent comparison, the S1 data were corrected (renormalized) to take into account the difference in FOV which is important when analyzing data in a region where the fluxes have a steep PAD (Borisov and Benck, 2019). Between January 2014 (top panel of Figure 10) and October/November 2014 (top panel of Figure 11), the situation has roughly not evolved. However, the layout of the SAA for channel 1 changes significantly from end 2014 (solar maximum, top

24

panel) to end 2019 (solar minimum, middle panel of Figure 11), with the southern region getting a strong enhancement in low energy protons. A factor 3 is observed at the northern edge of the SAA and around L=2 when comparing 2019 with 2014 (see red regions in Figure 11c). This increase is also visualized in Figure 12 where one (B, L) bin close to the valley has been chosen as illustration. This figure shows that the increase is continuous and not especially associated to specific events.

25
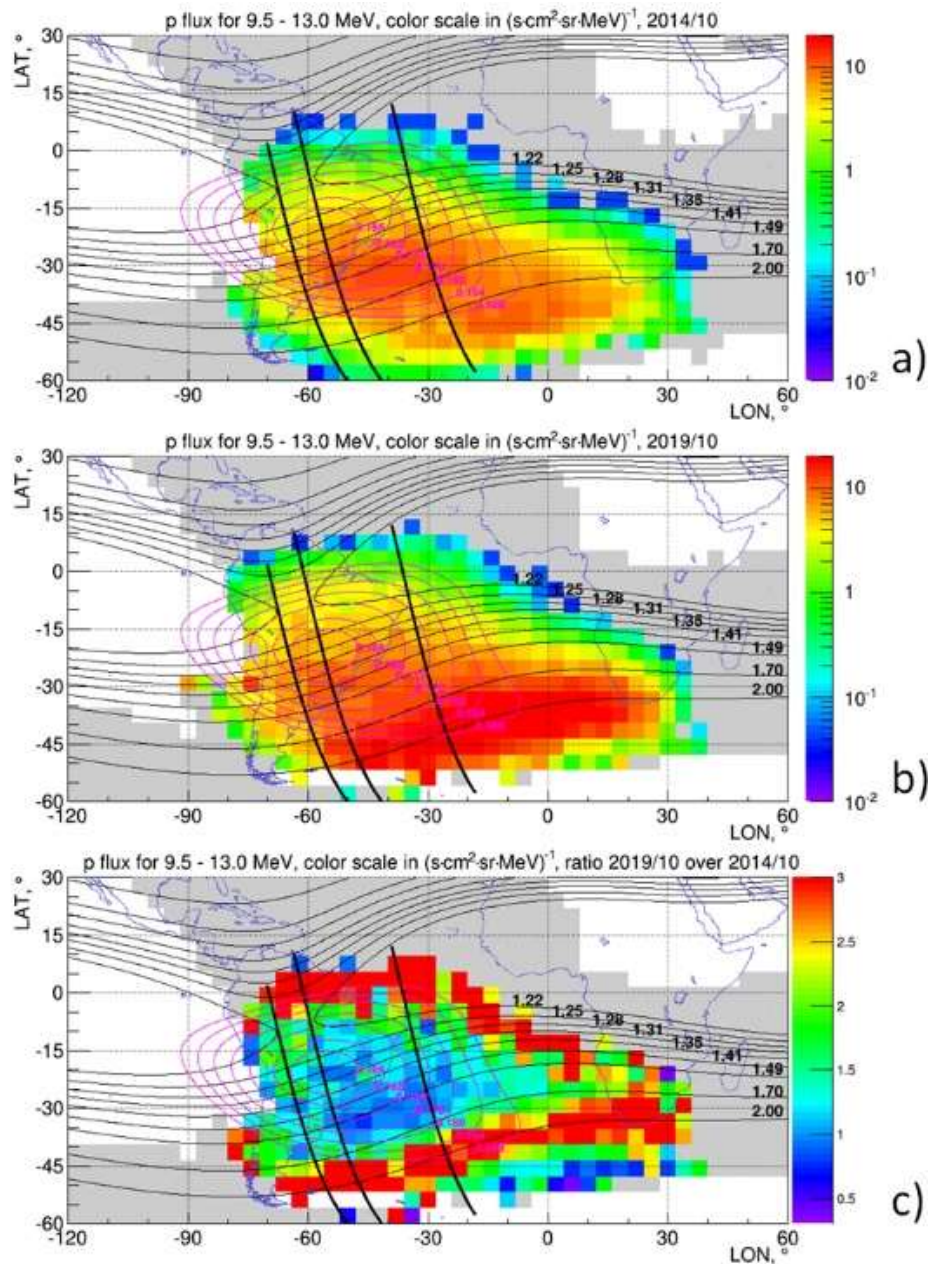
437 **Figure 11.** Geographical maps of the averaged proton flux in Ch 1: a) October and November 2014, b)
438 October and November 2019, c) ratio between 2019 and 2014 data. The bold black lines are parts of
439 trajectories showing how EPT crosses the SAA during night passes from south to north. The grey areas are
440 those where the fluxes are below minimum, i.e. 10^{-2} $s^{-1}cm^{-2}sr^{-1}MeV^{-1}$, and the white areas are those where
441 no data fulfill the selection criteria: night side data with boresight orientation $90°±10°$. Iso-L lines and iso-
442 B lines are shown by black and pink lines respectively.

443

444
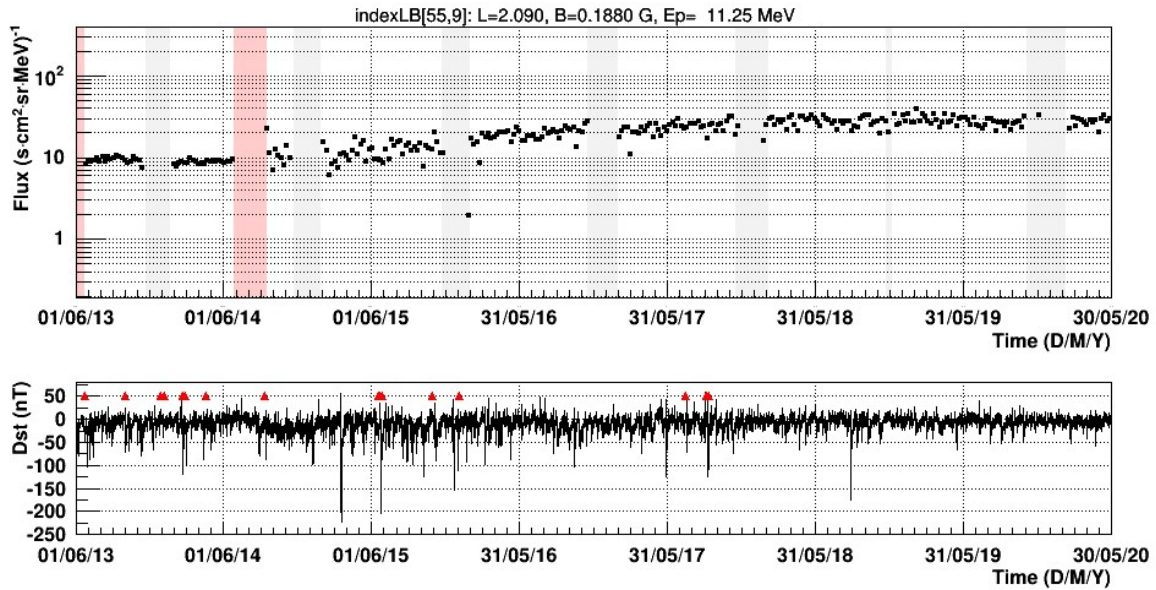
445 **Figure 12**. Time series of proton flux (weekly averages) in the SAA at one position in the southern part of
446 the SAA: L=2.09±0.01 and B=0.188±0.02 G. The fluxes present night-side data with boresight orientation
447 $90°±10°$ (upper panel). The bottom panel shows Dst as a function of time and the red triangles indicate the
448 occurrence of SEP events. The statistics in the flux data has changed after 15 September 2014 due to the
449 change in FOV (change in detector configuration, please see text), hence the increased data spread.

450 6 Discussion with respect to previous observations

451 Earlier satellites had detected multiple proton belts in the nineties. SAMPEX showed the formation
452 of several proton belts after the big SEP events of 1998 and 2000 (Heynderickx et al., 1999, Li et
453 al., 2020). CRRES observed that the March 1991 storm created a second, stable high energy belt
454 above *L*=1.8 for protons of 42 MeV, with peak flux values exceeding pre-storm values by an order
455 of magnitude (Albert et al., 1998). Intense fluxes of low energy protons down to L=1.35 were

26

456 reported by Parsignault et al. (1981) from 1972 to 1976. But it is the first time that the multiple

457 belts are associated to a splitting of the SAA and that they are observed recently and at LEO. The

458 advantage of EPT in comparison to other detectors at LEO is that it measures directly the

459 differential flux in a set of channels with a good defined FOV. Since these small-scale structures

460 may appear only for some specific energies, they cannot be easily detected in integral flux

461 measurements. Observations in regions of high energy radiation are particularly complicated due

462 to possible contaminations.

463 The NASA Van Allen Probes (VAP, also called Radiation Belt Storm Probes) mission (Mauk et

464 al., 2012) has been launched in 2012 and operated simultaneously with EPT. The data sets of EPT

465 and VAP allow to perform unprecedented studies of the radiation belt electron and proton

466 variability in response to solar activity and during the same periods of time. The orbit of VAP is

467 completely different from PROBA-V: VAP flied on a low inclination (10°) elliptical orbit ranging

468 from 600 to 30 600 km with a period of 9h and traversing the inner belt very quickly. Conjunction

469 regions only exist at L<1.5 (Pierrard et al., 2021). In addition to the different orbit, the proton

470 energy channels of REPT (Relativistic Electron Proton Telescope) (Selesnick et al., 2016) ranging

471 from 18 to 78 MeV are also different from EPT, complicating the direct comparison.

472 Close to the equatorial plane, the VAP/REPT fluxes for E < 32 MeV showed a two-peak structure

473 evolving with time with a valley located around L=1.7 (Selesnick and Albert, 2019). The fluxes

474 observed by VAP/REPT decrease with time from October 2013 to August 2015 at L<1.6 but

475 increase at L >1.7 corresponding to the second peak (see Figure 2 of Selesnick et al., 2016). An

476 increase in flux at L > 1.7 is also seen in EPT but only significant (due to statistical uncertainty)

477 when looking over a larger time frame (see Figure 11c southern part of the SAA for isolines

478 L>1.7).

479 In their study (Selesnick et al., 2016), REPT with its FOV of 32° was measuring protons with pitch

480 angles around 90°, i.e. the protons that mirror near the magnetic equator. Those protons were

481 measured at high altitude except when L<1.5 (possible conjunction region). On the other hand,

482 EPT mainly measures protons that have small equatorial PA as only those can reach low altitude.

483 The behavior of these protons may be different. For example, the equatorial mirroring protons

484 measured by REPT at L>1.2 are obviously not affected by solar cycle variation, i.e. the

485 atmospheric and ionospheric density. This is very different from measurements taken at highly

27

486 inclined LEO like PROBA-V/EPT that shows variation with solar cycle, as also confirmed by
487 SAMPEX or POES for instance (Li et al., 2020). Also, the observed flux variations are dependent
488 on L and B.

7   Conclusions

490 Since May 2013, the EPT spectrometer on-board PROBA-V provides high-resolution proton flux
491 measurements in the space environment of the Earth. In the present work, we analyze the long-
492 term and short-term evolution of the proton fluxes for different energy ranges and determine the
493 causes of the time variations to identify the mechanisms of sources and losses that influence their
494 changes with time. Very few clean measurements of differential proton fluxes at LEO are available
495 at different energy ranges above ~10 MeV during the last years. That is why EPT measurements
496 provide new results in this field, such as the splitting of the SAA observed for the energy <15 MeV
497 at LEO.

498 Indeed, only for Ch 1 (9.5 to 13 MeV), a stable double peak structure is observed by EPT with a
499 gap at L=2. This corresponds to a long-term splitting of the SAA in this energy range and a higher
500 extension of the south part of the SAA. Such a long-term splitting of the SAA at LEO was never
501 reported before and could be identified with the high-resolution measurements of differential
502 fluxes made by EPT.

503 In addition, analysis of long-time variations showed an anti-correlation (although time-shifted)
504 between the proton fluxes and the solar activity at all energies of EPT at the boarder of the SAA,
505 most strongly observed at L<1.25 and L~2.1. The low flux at low L in 2014 (solar maximum) can
506 be attributed to atmospheric loss at the lower edge of the proton belt. During the decreasing phase
507 till the solar activity minimum in 2019, the fluxes slightly increase due to the lower extension of
508 the atmosphere allowing to the protons to penetrate deeper. CRAND may also play a role, with
509 different effects depending on the energy and the L-shell.

510 SEP events increase the fluxes at high L during a few days, but do not inject fluxes in the SAA
511 during the period of observations of EPT (2013 to 2022). Nevertheless, the most intense
512 geomagnetic storms decrease the extension of the inner belt, best observable at the lowest energies.
513 This effect is particularly visible after the geomagnetic storm of March 2015 and the storm

appearing a few days after the beginning of the September 2017 SEP event. The arrival of many of such storms during the declining phase of the solar cycle may compensate somehow the flux increase due to the favorable atmospheric conditions (lower atmospheric loss) when solar minimum approaches. This effect is observed to be energy dependent.

8 Acknowledgements

Data Availability

EPT data are publicly available on the Space Situational Awareness website of ESA http://swe.ssa.esa.int/space-radiation. The list of the SEP events is available on https://umbra.nascom.nasa.gov/SEP/. Dst data was retrieved from https://wdc.kugi.kyoto-u.ac.jp/ and sunspot number data was downloaded from http://www.sidc.be/silso/datafiles/.

References

Albert, J. M., Ginet, G. P., and Gussenhoven, M. S. (1998), CRRES observations of radiation belt protons 1. Data overview and steady state radial diffusion, *J. Geophys. Res.: Space Physics*, 103, pp 9261-9274, doi: 10.1029/97JA02869.

29

Ameri, D., and Valtonen, E. (2019), Potential role of energetic particle observations in geomagnetic storm forecasting, Advances in Space Research, 64 (3), 801-813, doi: 10.1016/j.asr.2019.05.012

Baker, D.N., Erickson, P.J., Fennell, J.F., Foster, J.C., Jaynes, A.N., Verronen, P.T. (2018), Space Weather Effects in the Earth's Radiation Belts, *Space Science Reviews*, 214, 1, 17, 60 pp, doi: 10.1007/s11214-017-0452-7.

Benck, S., Borisov, S., Cyamukungu, M., Evans, H., Nieminen, P. (2016), Characterization of solar energetic H and He spectra measured by the Energetic Particle Telescope (EPT) on-board PROBA-V during the January 2014 SEP event, *IEEE Trans. on Nucl. Sci.*, 63, 6, 2941 – 2949, doi: 10.1109/TNS.2016.2610520.

Borisov, S., Benck, S., Cyamukungu, M., O'Brien, P., Mazur, J., Nieminen, P., Evans, H., and Daly, E. (2014), Angular Distribution of Protons Measured by the Energetic Particle Telescope on PROBA-V, *IEEE Trans. Nucl. Sci.*, 61, 6, 3371-3379, doi: 10.1109/TNS.2014.2361951.

Borisov, S., and Benck, S. (2019), Data analysis procedure for Proba-V/EPT spectra acquired after 15/09/2014, Technical Note 1B, Issue B, Review 1, 26/09/2019, Ref.: EPT-DEXT-TN-011-CS.

Cabrera, J., and Lemaire, J. (2007), Using invariant altitude (h(inv)) for mapping of the radiation belt fluxes in the low-altitude environment, Space Weather, 5, S04007, doi: 10.1029/2006SW000263.

Cyamukungu, M., Benck, S., Borisov, S. Bonnet, L., Grégoire, Gh., J. Cabrera, et al. (2014), The Energetic Particle Telescope (EPT) on board PROBA-V: description of a new science-class instrument for particle detection in space, *IEEE Trans. Nucl. Sci.*, 61, 6, 3667-3681, doi: 10.1109/TNS.2014.2361955.

Heynderickx, D., Kruglanski, M., Pierrard, V., Lemaire, J., Looper, M. D., and Blake, J. B. (1999), A low altitude trapped proton model for solar minimum conditions based on SAMPEX/PET data, *IEEE Trans. Nucl. Sci.*, 46, 1475-1480.

Jiggens, P., Clavie, C., Evans, H., O'Brien, T. P., Witasse, O., Mishev, A. L., Nieminen, P., et al. (2019), In Situ Data and Effect Correlation During September 2017 Solar Particle Event, *Space Weather*, 17, 1, 99-117.

30

569 Kruglanski, M. (1996), Engineering tool for trapped proton flux anisotropy evaluation, *Radiation*
570 *Measurements*, 26, 6, 953-958, doi: 10.1016/S1350-4487(96)00097-2.

571 Li, X., Selesnick, R. S., Zhao, H., Baker, D. N., Blake, J. B., and Temerin, M. A. (2021), Source,
572 Loss, and Transport of Energetic Particles Deep Inside Earth's Magnetosphere (L<4),
573 *Magnetospheres of the solar system*, Geophysical Monograph Series, Wiley Online Library, 323-
574 334, doi: 10.1002/9781119815624.ch21.

575 Li, X., Xiang, Z., Zhang, K., Khoo, L., Zhao, H., Baker, D. N., Temerin, M. A. (2020), New
576 Insights From Long-Term Measurements of Inner Belt Protons (10s of MeV) by SAMPEX, POES,
577 Van Allen Probes, and Simulation Results, *J. Geophys. Res.: Space Phys*., 125(8),
578 e2020JA028198, doi: 10.1029/2020JA028198.

579 Lopez Rosson, G., and Pierrard, V. (2017), Analysis of proton and electron spectra observed by
580 EPT/PROBA-V in the South Atlantic Anomaly, *Advances Space Res*., 60, 796-805, doi:
581 10.1016/j.as.2017.03.022.

582 Maget, V., Bourdarie, S., Rolland, G. (2013), Characterizing Solar Energetic Particles Access to
583 any Earth-Space Location, *IEEE Trans. Nucl. Sci.*, 99, 1-7, doi: 10.1109/TNS.2012.2233756.

584 Mauk, B. H., Fox, N. J., Kanekal, S. G., Kessel, R. L., Sibeck, D.G., and Ukhorskiy, A. (2012),
585 Science objectives and rationale for the Radiation Belt Storm Probes mission, *Space Sci Rev*, 179,
586 3–27, doi: 10.1007/s11214-012-9908-y.

587 McIlwain, C. E. (1966), Magnetic coordinates, *Space Science Rev*., 5, 585-598, doi:
588 10.1007/BF00167327.

589 Parsignault, A. M., Holeman, E., and Fizz, R. C. (1981), Long-term intensity decrease in the 8- to
590 25-MeV proton fluxes at low L values, *J. Geophys. Res.: Space Physics*, 86, 11447 – 11450.

591 Pierrard V., Botek, E., Ripoll, J.-F., and Cunningham, G. S. (2020), Electron dropout events and
592 flux enhancements associated with geomagnetic storms observed by PROBA-V/EPT from 2013
593 to 2019. *Journal of Geophysical Research: Space Physics*, 125, 12, e2020JA028487.

594 Pierrard V., Ripoll, J.-F., Cunningham, G., Botek, E., Santolik, O., Thaller, S., Kurth, W.,
595 Cosmides, M. (2021), Observations and simulations of dropout events and flux enhancements in

31

596   October 2013: Comparing MEO equatorial with LEO polar orbit, J. Geophys. Res.: Space Physics,
597   126, e2020JA028850, doi:10.1029/2020JA028850.

598   Pierrard, V., Lemaire, J., Heynderickx, D., Kruglanski, M., Looper, M., Blake, B., and Mewaldt,
599   D. (2000), Statistical analysis of SAMPEX/PET proton measurements, *NIM in Physics Research*,
600   449, 378 – 382.

601   Pierrard, V., and Lopez Rosson, G. (2016), The effects of the big storm events in the first half of
602   2015 on the radiation belts observed by EPT/PROBA-V. *Ann. Geophys.*, 34, 75-84, doi:
603   10.5194/angeo-34-75-2016.

604   Pierrard, V., Lopez Rosson, G., Borremans, K., Lemaire, J., Maes, J., Bonnewijn, S., Van
605   Ransbeeck, E. et al. (2014), The Energetic Particle Telescope: First results, *Space Science Rev*.,
606   184, 1, 87-106, doi: 10.1007/s11214-014-0097-8.

607   Pierrard V., Lopez Rosson, G. and Botek, E. (2019), Dynamics of Megaelectron Volt Electrons
608   Observed in the Inner Belt by PROBA-V/EPT, *J. Geophys. Res.: Space Physics*, 124, 1651-1659,
609   doi: 10.1029/2018JA026289.

610   Rouillard A.P., Viall N., Vocks C., Wu Y., Pinto R., Lavarra M., Matteini L., Pierrard V., Sanchez-
611   Diaz E., Alexandrova O., Lavraud B. (2021), The solar wind, Book Chapter in Solar Physics and
612   Solar wind, AGU Monograph, ed. Nour-Eddine Raouafi and Angelos Vourlidas, Vol. 1, 1-33,
613   doi: 10.1002/9781119815600.ch1

614   Selesnick, R. S., and Albert, J. M. (2019), Variability of the proton radiation belt, Journal of
615   Geophysical Research: Space Physics, 124, 5516–5527, doi: 10.1029/2019JA026754.

616   Selesnick, R. S., Baker, D. N., Jaynes, A. N., Li, X., Kanekal, S. G., Hudson, M. K., and Kress, B.
617   T. (2014), Observations of the inner radiation belt: CRAND and trapped solar protons, *J. Geophys.
618   Res.: Space Physics*, 119, 6541–6552, doi: 10.1002/2014JA02018.

619   Selesnick, R. S., Baker, D. N., Jaynes, A. N., Li, X., Kanekal, S. G., Hudson, M. K., and Kress, B.
620   T. (2016), Inward diffusion and loss of radiation belt protons, *J. Geophys. Res.: Space Physics*,
621   121, 1969–1978, doi: 10.1002/2015JA022154.

622 Selesnick R. S, Hudson, M. K., and Kress, B. T. (2010), Injection and loss of inner radiation belt

623 protons during solar proton events and magnetic storms, *J. Geophys. Res.: Space Physics*, 115,

624 A08211, doi: 10.1029/2010JA015247.

625 Vette, J. I. (1991), The NASA/National Space Science Data Center Trapped Radiation

626 Environment Model Program (1964-1991), *NSSDC/WDC-A-R&S 91-29*.

33